Estimating Marine Carbon Uptake in the Northeast Pacific Using a Neural Network Approach

Patrick J. Duke[1], Roberta C. Hamme[1], Debby Ianson[2,1], Peter Landschützer[3], Mohamed M. M. Ahmed[1,4], Neil C. Swart[5,1], Paul A. Covert[2]

[1]School of Earth and Ocean Sciences, University of Victoria, Victoria, BC, Canada
[2]Institute of Ocean Sciences, Fisheries and Oceans Canada, Sidney, BC, Canada
[3]Flanders Marine Institute (VLIZ), Ostend, Belgium
[4]Education and Research Group, Esri Canada, Calgary, AB, Canada
[5]Canadian Centre for Climate Modelling and Analysis, Environment and Climate Change Canada, Victoria, BC, Canada

Correspondence to: P. J. Duke (pjduke@ucalgary.ca)

Abstract. The global ocean takes up nearly a quarter of anthropogenic CO_2 emissions annually, but the variability of this uptake at regional scales remains poorly understood. Here we use a neural network approach to interpolate sparse observations, creating a monthly gridded seawater partial pressure of CO_2 (pCO_2) data product from January 1998 to December 2019, at $1/12°$x$1/12°$ spatial resolution, in the Northeast Pacific open ocean, a net sink region,. The data product (ANN-NEP; NCEI Accession 0277836) was created from pCO_2 observations within the 2021 version of the Surface Ocean CO_2 Atlas (SOCAT), and a range of predictor variables acting as proxies for processes affecting pCO_2 to create non-linear relationships to interpolate observations at a spatial resolution four times greater than leading global products and with better overall performance. In moving to a higher resolution, we show that the internal division of training data is the most important parameter for reducing overfitting. Using our pCO_2 product, wind speed, and atmospheric CO_2, we evaluate air-sea CO_2 flux variability. On sub-decadal to decadal timescales, we find that the upwelling strength of the subpolar Alaskan Gyre, driven by large-scale atmospheric forcing, acts as the primary control on air-sea CO_2 flux variability ($r^2 = 0.93$, $p < 0.01$). In the northern part of our study region, divergence with atmospheric CO_2 is enhanced by increased local wind stress curl, enhancing upwelling and entrainment of naturally CO_2-rich subsurface waters, leading to decade-long intervals of strong winter outgassing. During recent Pacific marine heatwaves from 2013 on, we find enhanced atmospheric CO_2 uptake (by as much as 45%) due to limited wintertime entrainment. Our product estimates long-term surface ocean pCO_2 increase at a rate below the atmospheric trend (1.4 ± 0.1 μatm yr^{-1}) with the slowest increase in the center of the subpolar gyre where there is strong interaction with subsurface waters. This mismatch suggests the Northeast Pacific Ocean sink for atmospheric CO_2 may be increasing.

1 Introduction

As countries around the world consider updating their carbon emission reduction commitments (United Nations Environment Programme, 2022), we require a better understanding of global carbon sinks and how they may be shifting under climate change. The global ocean takes up nearly a quarter of anthropogenic carbon dioxide (CO_2) emissions annually (Friedlingstein et al., 2022) but the temporal and spatial variability of the marine sink remains unclear on decadal or longer timescales

(McKinley et al., 2011; Fay and McKinley, 2013; Wanninkhof et al., 2013; Gruber et al., 2023). Potential future changes in the marine sink associated with climate change are also unclear (O'Neill et al., 2018). Extending the spatial and temporal coverage of partial pressure of CO_2 in seawater (pCO_2) observations can help address this knowledge gap (Aricò et al., 2021). Benefitting from the increasing abundance of CO_2 measurements at sea and community synthesis efforts (e.g., through the Surface Ocean CO_2 Atlas (SOCAT)), a variety of interpolation approaches have evolved capable of creating continuous observation-based estimates of pCO_2 (Denvil-Sommer et al., 2019; Zhong et al., 2022; Laruelle et al., 2017; Nakaoka et al., 2013; Chen et al., 2019; Ritter et al., 2017; Landschützer et al., 2013). However, their global focus and coarse resolution limits their interpretation at regional scales (Olivier et al., 2022). Only recently, higher resolution regional pCO_2 maps have been developed for the California current system (Sharp et al., 2022) to overcome the limitations of coarse global scale pCO_2 products. These seawater pCO_2 products, combined with wind speed and atmospheric pCO_2, have informed regional to global air-sea CO_2 flux estimates of multiyear variability (Landschützer et al., 2019, 2016, 2015; Wang et al., 2021; Hauck et al., 2020).

No high-resolution observation-based air-sea CO_2 flux estimate currently exists for the North Pacific Ocean. The Northeast Pacific Ocean has been characterized as a net annual sink for atmospheric CO_2 (Wong et al., 2010; Franco et al., 2021; Sutton et al., 2017; Duke et al., 2023b). The region is divided by two dominant oceanographic features, the Alaskan Gyre system to the north, and the North Pacific Current to the south (Franco et al., 2021). With respect to surface ocean carbon measurements, the Alaskan Gyre system remains extremely sparsely sampled. The seasonal air-sea CO_2 flux of the gyre has been described as being strongly influenced by gyre upwelling with outgassing in the winter and uptake in the summer (Brady et al., 2019; Palevsky et al., 2013; Chierici et al., 2006). Along the easternmost part of the North Pacific Current, most of our understanding comes from a limited region; the Ocean Station Papa mooring at 50°N, 145°W (Sutton et al., 2017), and the Line P program (Freeland, 2007). This region has well documented seasonal cycles (Sutton et al., 2017), interannual variability (Wong and Chan, 1991; Wong et al., 2010), and long-term trends (Franco et al., 2021; Sutton et al., 2019). CO_2 uptake is mainly driven by direct ventilation of the shallow upper water column, with a small seasonal change in surface ocean pCO_2 (Wong et al., 2010; Sutton et al., 2017). The estimated long-term trend in surface ocean pCO_2 appears to be increasing at less than the atmospheric rate of increase (Franco et al., 2021).

Understanding what drives air-sea CO_2 fluxes on seasonal, interannual, and decadal timescales in the Northeast Pacific Ocean will inform how the regional sink may change in future. This region is already experiencing persistent marine heatwaves with dramatic temperature anomalies observed during 2014 to 2016 and 2018 to 2020 events (Freeland and Ross, 2019; Bond et al., 2015), with future events predicted to become longer-lasting, more frequent, more extensive, and more intense (Frölicher et al., 2018). The impact of large-scale climate-driven decadal oscillations on the marine carbon system is just beginning to be explored in models (Hauri et al., 2021). Furthermore, this region has been targeted as a potential site of marine carbon dioxide removal, as a negative emissions technology aimed at meeting emission reduction goals continues to grow in interest and investment (Cooley et al., 2022). Some proposed approaches look to artificially stimulate biological carbon drawdown (GESAMP, 2019; NASEM, 2021). The Northeast Pacific Ocean, as an iron-limited high-nutrient low-chlorophyll region

(Dugdale and Wilkerson, 1991; Aumont et al., 2003; Martin et al., 1994; Freeland et al., 1984), has already been the location of geoengineered biological carbon drawdown experiments (Boyd et al., 2007, 2005; Wong and Johnson, 2002; Ianson et al., 2012). Thus, a firm understanding of processes driving carbon fluxes and the establishment of environmental baselines in the region is critical.

Our aim is to investigate drivers of air-sea CO_2 flux variability in the Northeast Pacific (NEP) Ocean, building a novel regional high-resolution artificial neural network (ANN) approach adopted from an existing global setup (Landschützer et al., 2013). In Section 2, we describe the creation of a gridded pCO_2 data product (herein referred to as ANN-NEP; NCEI Accession 0277836; Duke et al., 2023a) monthly from January 1998 to December 2019 at $1/12°x1/12°$ spatial resolution in the Northeast Pacific open ocean (approximately 9 km by 5km; latitude by longitude). In Section 3, we show that the high-resolution regional pCO_2 product is robust enough to recreate training observation data while generalizing well compared to independent withheld observation data. We also show that stepping to a higher resolution regionally with appropriate tuning of the internal training and evaluation data ratio does not hinder product performance. In Section 4, our results show that the upwelling strength of the subpolar Alaskan Gyre and surface ocean connectivity to subsurface waters act as the primary control on air-sea CO_2 flux variability in our study area. We conclude by calculating long-term trends in surface ocean pCO_2 and carbon uptake, examining trends relative to connectivity to subsurface waters.

2 Data and methods

Our study area comprises the region between latitudes 45°N and 62°N and longitudes 120°W and 155°W (Figure 1), with the open-oceanic/coastal boundary defined as 300 km offshore following Laruelle et al. (2017). We limit our study region to the open ocean regions with reduced variability and related drivers compared to the continental shelf regions. Creating a product on the continental shelf and in the nearshore requires different neural network considerations and is associated with high uncertainties (Roobaert et al., 2023). This work represents a four times increase in spatial resolution over previous multiyear global open ocean products, usually coarser than $1/4°$ (Landschützer et al., 2020b). The increased resolution derives from high-resolution predictor data used to create the product (Table 1). To interpolate the existing CO_2 observations in this domain, we adapt the artificial neural network (ANN) self-organizing-map-feed-forward-network (SOM-FFN) approach developed by Landschützer et al. (2013, 2014). In a first step, the method divides the region of interest into dynamic zones with similar biogeochemical features (i.e., SOM biogeochemical provinces), using a self-organizing map approach. In a second step, a feed-forward neural network is used for interpolating pCO_2 observations in each of the pre-determined provinces of step one. Specifically, non-linear functional relationships are created between pCO_2 observations (or neural network target data), where they exist in our study domain, and independent predictor variables (or neural network input data) that are known to drive the marine carbon cycle (see Section 2.1 below). Once the relationships are established, they can be applied where no observations exist to fill space/time gaps and create continuous sea surface pCO_2 maps from 1998-2019.

2.1 Predictor data

The chosen predictor variables for this study (Table 1) had all been used previously in observation-based pCO$_2$ interpolated
100 products (Denvil-Sommer et al., 2019; Zhong et al., 2022; Landschützer et al., 2014; Gregor et al., 2018; Telszewski et al., 2009). Sea surface temperature (SST) comes from the satellite-based European Space Agency Climate Change Initiative (Merchant et al., 2019; ESA Sea Surface Temperature Climate Change Initiative (SST_cci): Level 4 Analysis Climate Data Record, version 2.1), as well as Chlorophyll-a concentration which served as a proxy for biological processes (ESA Ocean Colour Climate Change Initiative (Ocean_Colour_cci): Global chlorophyll-a data products gridded on a geographic projection,
105 Version 5.0). Remaining physical process predictor data (e.g., sea surface salinity (SSS), sea surface height (SSH), and mixed layer depth (MLD)) are obtained from Copernicus Marine Environment Monitoring Service global ocean eddy-resolving reanalysis (Global Ocean Physical Reanalysis Product, E.U. Copernicus Marine Service Information GLOBAL_REANALYSIS_PHY_001_030). Jointly assimilated observations include satellite altimeter data and *in situ* vertical profiles of temperature and salinity informing the MLD reanalysis product (Table 1). The ocean general circulation model is
110 based on the Nucleus for European Modelling of the Ocean (NEMO) platform, driven at the surface by the European Centre for Medium-Range Weather Forecasts ERA-Interim winds (Jean-Michel et al., 2021). Both Chlorophyll-a and mixed layer depth were log10-transformed to produce a distribution of values closer to normal before being used in either SOM-FFN step. Atmospheric pCO$_2$ in µatm was downloaded from (Landschützer et al.~~,~~ (2020b), derived from the National Oceanic and Atmospheric Administration Earth System Research Global Monitoring Laboratory (https://gml.noaa.gov/ccgg/globalview/)
115 atmospheric mole fraction of CO$_2$ (χCO$_2$) and SST (Reynolds et al., 2002) as well as sea level pressure (Kalnay et al., 1996) following (Dickson et al.~~,~~ (2007)~~Atmospheric mole fraction of CO$_2$ (χCO$_2$) is derived from data produced by National Oceanic and Atmospheric Administration Earth System Research Global Monitoring Laboratory (https://gml.noaa.gov/ccgg/globalview/)~~. Finally, the monthly pCO$_2$ climatology of Landschützer et al. (2020) was used as an additional input parameter solely for defining the SOM biogeochemical provinces.

120 ## 2.2 pCO$_2$ observations

ANN target pCO$_2$ data come from the Surface Ocean CO$_2$ Atlas (SOCAT) v2021 (Bakker et al., 2016), as well as additional data from the Fisheries and Oceans Canada February 2019 Line P cruise (https://www.waterproperties.ca/linep/; Figure 1c). Sea surface CO$_2$ fugacity (fCO$_2$) was converted to sea surface pCO$_2$ (supplementary Text 1; Körtzinger, 1999). pCO$_2$ observations were bin-averaged into monthly, 1/12° latitude by 1/12° longitude grid cells computing the mean and standard
125 deviation within each grid cell. Of the 8,712,264 grid cells that represent the surface ocean gridded in three dimensions over 264 months (1998–2019) at 1/12°x1/12° resolution in the study area, just 0.39% have an associated gridded pCO$_2$ value (Figure 1).

2.3 Evaluation

In constructing the optimal ANN architecture, a series of SOM-FFN tuning tests were conducted comparing ANN output to
130   training and independent withheld data. ANN performance for each tuning test was evaluated using five statistical metrics:
root mean squared error (RMSE), coefficient of determination (r^2), mean absolute error (MAE), mean bias (calculated as the
mean residual), and the slope of the linear regression (c_1) between the ANN and the corresponding gridded SOCAT pCO_2
observations. Independent withheld data came from randomly selected SOCAT data using associated expocodes corresponding
to unique complete underway cruise tracks or mooring deployments. We tested 100 random independent withheld data splits
135   and selected one representative of basin-wide observational coverage (summer/southern sampling bias), with winter, spring,
and fall data present (Figure 1; supplementary Figure 1). These independent withheld data represented approximately 5% of
the total study area gridded pCO_2 data, with coverage during all seasons over a range of latitudes (supplementary Figure 1).
Ensuring selected independent withheld data is random, yet also representative of the full domain, without withholding critical
end range training data is difficult. Community-based best practices are likely needed going forward to ensure continuity in
140   reported observation-based pCO_2 product uncertainty.

2.4 Neural network construction

SOM-FFN tuning tests occurred in series using the MATLAB Neural Network Toolbox, with sequential improvements
impacting future tests. Optimization of the SOM-derived biogeochemical provinces involved trial-and error testing of various
parameters including SOM biogeochemical province count, predictor variables choice, and static or varying province shape
145   with each timestep (Landschützer et al., 2013). The choice of four SOM biogeochemical provinces represented the lowest
number of SOM biogeochemical provinces for a typical clustering structure to emerge (supplementary Figure 2), while keeping
the ratio of gridded pCO_2 observation to the total grid cells within each province similar (0.38±0.06%). The best SOM predictor
variables were SST, SSS, MLD (Table 1), and the Landschützer et al. (2020a) pCO_2 climatology. We did not normalize
predictor data (e.g., force a mean of 0 and standard deviation of 1), implicitly weighting SOM predictors toward the pCO_2
150   climatology as its range is at least one order of magnitude greater than that for SST, SSS, and log(MLD) (Landschützer et al.,
2013) as was done in Landschützer et al. (2013). As a result, our dynamic provinces follow the seasonal variations in the pCO_2
climatology (Landschützer et al., 2020a). Thus, non-static provinces, that changed shape from one month to the next over a
climatology, proved the most useful in clustering seasonal cycle variability. This clustering does lead to clearly unphysical
fronts as an artifact of the approach.
155   In reaching an optimal FFN architecture (i.e., number of inputs, number of hidden layers and neurons in each hidden layer),
trial-and error testing of tuning parameters explored predictor variable choice, FFN training algorithm and activation functions,
pre-training to determine the number of neurons in the first hidden layer, introducing a second hidden layer with a static number
of neurons, and changing the internal data division ratio (94:6; see Section 3.4 below).

To emphasize interannual and longer-term trends within the six predictor variables (Table 1), each predictor variable is used in two different forms, first in its raw form and second after deseasonalizing, bringing the total number of FFN predictors used to 12~~To emphasize interannual and longer term trends within predictor variables (Table 1), we introduced each predictor variable again after deseasonalizing~~. To deseasonalize, within~~For~~ each grid cell, the monthly anomaly was calculated by subtracting the climatological monthly mean, removing the seasonal cycle from the data (the same approach is used when looking at anomaly values in our results; Section 4). Where no chlorophyll-a satellite data were available, the ANN was run again with the remaining predictors and output was merged to fill empty grid cells (Landschützer et al., 2014). The Levenberg–Marquardt backpropagation training algorithm and hyperbolic tangent sigmoid activation function (i.e., trainlm and tansig respectfully in MATLAB) were found to deliver the best fit. The number of neurons within the first hidden layer varied by province and the optimal number of neurons was determined in a pre-training run, where we increased the number of neurons parabolically from two up to a number where the ratio between the training sample size to the number of weights did not exceed 30 (i.e., a number that was determined by trial and error). The best output performance of the pre-training determines the best neuron setup which was then further used for the actual ANN training.

To avoid overfitting, we split all the internal training data into two subsets (i.e., one actual training dataset and one internal evaluation dataset). While most studies use a fixed ratio (usually 80:20) between these sets, we used the optimal ratio determined by a criterion suggested in Amari et al. (1997) that is dependent on the number of degrees of freedom and hence varies with the optimal number of neurons determined in the pre-training (see Section 3.4 below). While the training dataset is used to reconstruct the non-linear relationship between input data (Table 1) and pCO$_2$ observations, the internal evaluation data are used to stop the training before the network starts overfitting the training data. Specifically, we stopped the training when 6 consecutive iterations did not reduce the network's error compared to internal evaluation data (Hsieh, 2009). The addition of a second hidden layer with a static neuron number of five was found to slightly improve performance within the evaluation metrics.

2.5 Cross-evaluation and ensemble

In order to further decrease the risk of overfitting, we used a 10-fold cross-evaluation approach (Li et al., 2019, 2020) and a bootstrapping method (Landschützer et al., 2013). Here, all SOCAT cruises (apart from the independent withheld data; Section 2.3) were randomly divided into ten equal subsamples using SOCAT expocodes prior to gridding. One subsample was used as 10-fold evaluation data (10% of all data), and was excluded from training, while the remaining nine subsamples were used together as training data (90% of all data). The cross-evaluation process was repeated ten times, with each of the ten subsamples used exactly once as the 10-fold evaluation dataset. We performed ten trainings with each 10-fold training data subsample where we randomly split the ANN internal training and evaluation data based on the optimal ratio determined through testing (Section 3.4). The robustness and reliability of an ANN has been shown to be significantly improved by combining several ANNs into an ANN ensemble model (Sharkey, 1999; Linares-Rodriguez et al., 2013; Fourrier et al., 2020). The ten different

ANN outputs trained on ten different 10-fold training data subsamples were used as an ANN ensemble, where the ten outputs were averaged to obtain the final ANN-NEP $p\text{CO}_2$ product (Fourrier et al., 2020).

2.6 Computation of air-sea fluxes

Using the ANN-NEP $p\text{CO}_2$ product, the air-sea CO_2 flux ($F\text{CO}_2$), was calculated using Eq. 1:

$$F\text{CO}_2 = \propto k\Delta p\text{CO}_2 , \tag{1}$$

based on solubility ($\propto$) as a function of temperature and salinity using the data presented in Table 1 (Weiss, 1974), gas transfer velocity (k), and the gradient between $p\text{CO}_2$ in the surface ocean and the atmosphere ($\Delta p\text{CO}_2$). Here, the gas transfer velocity is a function of wind-speed retrieved from monthly, 1/4° spatial resolution Cross-Calibrated Multiplatform ocean surface wind data (Mears et al., 2019) interpolated to 1/12°, the temperature dependent Schmidt number specific to CO_2, and gas transfer coefficient from Wanninkhof (2014). Negative (positive) flux values indicate CO_2 uptake (outgassing) by the ocean. Uncertainty in the air-sea CO_2 flux comes from a 20% uncertainty in k (Wanninkhof, 2014) and the overall product uncertainty in estimated $p\text{CO}_2$ ($\theta_{p\text{CO}2}$; Eq. 2; see Section 3.2 below). As the uncertainty of $\Delta p\text{CO}_2$ is dominated by the uncertainty in estimated surface ocean $p\text{CO}_2$, we neglect the small contribution from atmospheric CO_2 (<1 µatm; Landschützer et al. 2014).

3 Network performance

3.1 Evaluation comparing to SOCAT data

Overall, the final high-resolution regional artificial neural network Northeast Pacific $p\text{CO}_2$ product (ANN-NEP) obtains good fits with an overall r^2 of better than 0.8 and RMSE of around 11 µatm between the estimated $p\text{CO}_2$ and the gridded SOCAT $p\text{CO}_2$ data across both the training data (Figure 2a), and independent withheld data (Figure 2b). The mean bias is negligible (<0.8 µatm; smaller than observational uncertainty). These results also apply within individual calendar years, and within monthly groupings across all years, indicating that the temporally inhomogeneous data distribution over the time range and between seasons does not have a measurable effect on the estimates (supplementary Table 1). There is no clear spatial structure to the residuals, with no specific region displaying persistently positive or negative residuals (supplementary Figure 3). When compared to local $p\text{CO}_2$ mooring data from Ocean Station Papa (which is included in SOCAT; Figure 1; Sutton et al. 2017), the ANN-NEP product also performs well ($r^2 = 0.86$; 133 months; not shown).

The ANN ensemble model mean approach demonstrated improved performance metrics when compared to each individual ensemble member. The ensemble median was nearly equivalent to the ensemble mean ($r^2 = 0.99$; not shown). Overall, individual ensemble members showed little deviation (RMSE <8 µatm) from the ensemble mean (Figure 2c), with the ensemble mean still improving estimate robustness and reducing overtraining as evident in comparing the final ANN product to independently withheld data (Figure 2b) and the mean RMSE of individual ensemble members to independently withheld

220   data (13±1 µatm; supplementary Figure 4a). Each individual ensemble member also performed relatively well compared to the 10% subsample of corresponding 10-fold evaluation data (mean RMSE = 17±2 µatm; supplementary Figure 4b). The mean standard deviation across all grid cells within the 10-fold ensemble is 2.2±1.3 µatm (mapped in supplementary Figure 5).

3.2 Uncertainty calculations

Uncertainty in the ANN estimated pCO_2 product was calculated following Landschützer et al. (2018, 2014), Roobaert et al.
225   (2019), and Keppler et al. (2020) (Eq. 2), where the overall pCO_2 product uncertainty (θ_{pCO2}) is calculated from the square root of the sum of the four squared errors: observational uncertainty (θ_{obs}), gridding uncertainty (θ_{grid}), ANN interpolation uncertainty (θ_{map}), and ANN run randomness uncertainty (θ_{run}).

$$\theta_{pCO2} = \sqrt{\theta_{obs}^2 + \theta_{grid}^2 + \theta_{map}^2 + \theta_{run}^2}, \tag{2}$$

Observational uncertainty ($\theta_{obs} = 3.1$ µatm) is the measurement uncertainty of pCO_2 in the field, evaluated as the average of
230   the uncertainty assigned to each data point according to its SOCAT quality control (QC) flag (between 2-5 µatm). Gridding uncertainty ($\theta_{grid} = 1.5$ µatm) is associated with gridding SOCAT observations into monthly $1/12°\times1/12°$ bins, evaluated as the average standard deviation among pCO_2 values within each grid cell with at least 3 data points. ANN interpolation uncertainty ($\theta_{map} = 11.1$ µatm) is uncertainty introduced by interpolating the pCO_2 observations using the SOM-FFN approach, evaluated as the RMSE from the ANN ensemble output compared to the independent withheld SOCAT data (Figure 2b). One
235   limitation of our approach in assessing the uncertainty of the ANN interpolation method is that it is only applicable to grid cells where observations are available. Consequently, location-specific seasonal biases, especially in high latitudes with limited wintertime observations (Figure 1a&b), may not be fully captured or accounted for. The standard deviation of the ensemble (ensemble spread) gives an indication of how robust our estimate is from one run to the next using different 10-fold training data (Section 2.5; Keppler et al., 2020). ANN run randomness uncertainty ($\theta_{run} = 2.2$ µatm) comes from the mean standard
240   deviation between 10-fold ensemble members (Section 2.5 & 3.1), which is less than the comparison of each member of the ensemble with the ensemble mean (supplementary Figure 4; Figure 2c).

Overall product uncertainty combining all four components according to Eq. (2) is 12 µatm, with the contribution of ANN interpolation uncertainty being the largest. Our product uncertainty is comparable to reported open ocean uncertainty values from global products (Landschützer et al., 2014), as well as a regional product in the California Current System (Sharp et al.,
245   2022). Combining the reported uncertainty in the gas transfer velocity (Section 2.6) and the overall pCO_2 product uncertainty yields an average uncertainty of ±0.24 mol m^{-2} yr^{-1} in the air-sea gas flux, with the largest fraction of the error stemming from the uncertainty of the gas transfer velocity. The total uncertainty in the flux corresponds to roughly 20% of individual grid cell calculated flux values.

3.3 Improvement relative to a global product

250   The ANN-NEP pCO_2 product created here shows improved performance over the Landschützer et al. (2020b) global product at each timestep within the study area when compared to SOCAT data gridded at $1/12°x1/12°$ (Figure 3), illustrating the importance of regional high-resolution estimates in resolving fine scale variations. Across all evaluation metrics the global product does not perform as well in the region compared to SOCAT training data (RMSE = 14; r^2 = 0.74; mean bias = -2; c_0 = 0.68; MAE = 10; compared to Figure 2a). This improvement suggests a regional high-resolution product can narrow the

255   range of variability in predictor data within the SOM clustering step and present pCO_2 observation data with greater correlation to the FFN. In the Landschützer et al. (2020b) global product, there is often only one SOM biogeochemical province covering the whole region, forcing non-linear relationships in the FFN to be built around greater variability in pCO_2 observation data from a wider range of geographic areas. The ANN-NEP regionally specific four SOM biogeochemical province grouping could alleviate this shortcoming in the FFN step. The improvement in our high-resolution product is particularly evident in the

260   seasonal amplitude, where differences between ANN-NEP and Landschützer et al. (2020b) exceed the product uncertainty in 25% of grid cells (supplementary Figure 6a). The largest seasonal amplitude differences occur in the north Alaskan Gyre region, and south of the North Pacific Current (supplementary Figure 6b). The additional spatial resolution and temporal details in the regional high-resolution product provide key information to inform future observation programs including potential mooring locations. The value added in stepping to a high-resolution regional product proves particularly useful in resolving

265   biogeochemical gradients within the subpolar Alaskan Gyre system in our study area (Section 4).

3.4 Performance at coarser resolutions

Stepping to a higher spatial resolution drastically decreases the ratio of gridded pCO_2 observations compared to the total number of grid cells (Figure 4f), nevertheless the ANN experiences minimal loss in performance across different spatial resolutions (Figure 4a-e). Globally, most open ocean observation-based pCO_2 products interpolate on a $1°x1°$ gridded

270   resolution (Landschützer et al., 2020b; Global Ocean Surface Carbon, E.U. Copernicus Marine Service Information MULTIOBS_GLO_BIO_CARBON_SURFACE_REP_015_008; Denvil-Sommer et al., 2019; Zhong et al., 2022), with most coastal or regional products using a $1/4°x1/4°$ grid cell size (Laruelle et al., 2017; Sharp et al., 2022; Hales et al., 2012; Nakaoka et al., 2013), with a few regional products stepping to even higher resolutions (e.g., 1-km in Chen et al. 2016; 4-km in Parard et al. 2015, 2016; 11-km in Xu et al. 2019). To determine how the network preforms when producing a coarser resolution

275   product, we tested the same configuration of our tuned $1/12°x1/12°$ ANN at various resolutions (Figure 4). The predictor variables and SOCAT pCO_2 observations were simply bin-averaged to coarser grid cell sizes (i.e., 1°, 1/2°, 1/4°, 1/8°).

Using the same ANN configuration between the different resolutions (i.e., optimal SOM biogeochemical provinces, appropriate predictors, neuron number in the first hidden layer, etc., see Section 2.5), the most important parameter for reducing overfitting at each resolution becomes the internal data division ratio between the pCO_2 training data used by the ANN to train

280   and internally evaluate (Figure 4). We tested a suite of data division ratios between 99% of data used to train / 1% used to

internally evaluate to a 50/50 split at 1% intervals for each resolution (Figure 4). These tests were run without the 10-fold cross-evaluation ensemble approach. To quantify the optimal ratio at each resolution, we used an overfitting metric (Eq. 3) equal to the larger of the training or independently withheld data RMSE, plus the absolute value of the difference between the two:

285 $$\text{Overfitting metric} = \max\left(\text{RMSE}_{training}, \text{RMSE}_{withheld}\right) + \left|\text{RMSE}_{training} - \text{RMSE}_{withheld}\right|, \tag{3}$$

Using an internal data division ratio optimized based on the overfitting metric, an ANN interpolated pCO_2 product with an uncertainty value of 12.5±0.4 µatm (see Section 3.2; supplementary Table 2) is possible at each of the coarser resolutions (Figure 4a-e; supplementary Table 2). For comparison, the reported uncertainty in a global product (Landschützer et al., 2014) ranges from 9 to 18 µatm. In regions with sufficient observational coverage (Figure 4f; Bakker et al., 2016), this finding creates

290 a precedent for stepping to a higher resolution product with nearly no loss in performance, overcoming the overfitting concern with increased resolution (Rosenthal, 2016).

4 Air-sea CO₂ fluxes

With the estimated ANN pCO_2 product displaying a strong ability to accurately represent regional pCO_2 variability in the Northeast Pacific (Section 3), we calculate air-sea CO_2 fluxes in the region (Eq. 1). Long-term (1998-2019) mean pCO_2 and

295 air-sea CO_2 fluxes display similar patterns (Figure 5). In the northwest of our study area, high pCO_2 and net CO_2 outgassing to the atmosphere correspond to the influence of the upwelling subpolar Alaskan Gyre system (Figure 5; Figure 1c). Lower pCO_2 values and stronger atmospheric CO_2 uptake occur in the North Pacific Current region (Figure 1c) to the south and along the eastern study area margin (Figure 5). The gradient of the gyre captured in the high-resolution estimate improves regional understanding with the largest differences between the Landschützer et al. (2020b) global product occurring in the north (basin-

300 wide absolute difference 2-5%; supplementary Figure 6a). ANN-NEP calculated fluxes compare well to air-sea CO_2 fluxes averaged across six unique, courser resolution, global observation-based pCO_2 products, each using five different wind speed products ($r^2 = 0.81$; (Fay et al., 2021). However, our work suggests that the global product ensemble may underestimate the outgassing signal from the subpolar Alaskan Gyre (Figure 5b; supplementary Figure 7). Higher resolution in the gyre gradient also provides regional context to carbon measurements made at the Ocean Station Papa mooring, often used to represent the

305 Alaskan gyre (e.g., Jackson et al. 2009), which is actually situated approximately between the two regions, and along the Line P monitoring program.

4.1 Seasonal variability

To determine seasonal cycle drivers, we decompose the climatological pCO_2 into a thermal and non-thermal component (Takahashi et al., 2002, 1993):

310 $$pCO_{2\ (T)} = pCO_{2\ (am)} \times \exp\left[0.0423\left(T_{(mm)} - T_{(am)}\right)\right], \tag{4}$$

$$pCO_{2\,(NT)} = pCO_{2\,(mm)} \times \exp\left[0.0423\left(T_{(am)} - T_{(mm)}\right)\right], \tag{5}$$

$$R_{(T\,NT^{-1})} = \frac{\max(pCO_{2\,(T)}) - \min(pCO_{2\,(T)})}{\max(pCO_{2\,(NT)}) - \min(pCO_{2\,(NT)})}, \tag{6}$$

Here the subscripts T and NT represent thermal and non-thermal effects, respectively, while subscripts am and mm represent annual mean and monthly mean values, respectively. Eq. 4 imposes the empirical temperature dependency on the annual mean
315   pCO_2 value providing an estimate of seasonal temperature control (Sarmiento and Gruber, 2006; Takahashi et al., 2002). Eq. 5 removes the temperature dependency from the monthly mean pCO_2 values providing an estimate of the residual, non-thermal controls on pCO_2 including circulation, mixing, gas exchange, and biology. The ratio of the seasonal amplitudes of the two components (Eq. 6; $R_{(T\,NT^{-1})}$) can differentiate the dominant process, where a value greater (less) than one indicates that thermal (non-thermal) processes dominate.

320   Seasonally, the northern Alaskan Gyre region of our study area (latitudes north of 52°N; Figure 6a&b), flips from outgassing in the wintertime to uptake in the summer in the climatological air-sea CO_2 flux (Brady et al., 2019; Palevsky et al., 2013; Chierici et al., 2006). The change in the sign of the flux is driven by a 40 µatm difference between winter maxima and summer minima pCO_2 climatology values (Figure 6b). In the Landschützer et al. (2020a) climatology, this seasonal dipole in the Alaskan Gyre also exists displaying a 40 µatm seasonal pCO_2 range. Similar patterns exist in the Takahashi et al. (2014, 2009,
325   2002) climatologies as well (approximately 45-50 µatm). Increased wind stress curl drives stronger gyre circulation in the fall and winter, upwelling and entraining nutrient and CO_2-rich subsurface waters into the surface ocean, increasing the non-thermal pCO_2 component (Figure 6b), leading to outgassing (Figure 6a; Chierici et al. 2006). Through the spring and summer, biological drawdown, preconditioned by the upwelled, mixed, and entrained nutrients, decrease the surface ocean non-thermal pCO_2 component (Figure 6b; Harrison et al. 1999), enhancing uptake (Figure 6a). Although the seasonal amplitude of the
330   temperature component is also large in the north, these non-thermal controls dominate ($R_{(T\,NT^{-1})} = 0.84$).

In the south part of our study area, the North Pacific Current region (latitudes south of 52°N; Figure 6a&c) acts as a strong CO_2 sink through the winter transitioning to a weak sink through the summer. Whereas in the Alaskan Gyre region the seasonal cycle of pCO_2 is dominantly controlled by non-thermal drivers (Figure 6b), the North Pacific Current region experiences a near balance between opposing drivers (Figure 6c; $R_{(T\,NT^{-1})} = 1.02$). In the North Pacific Current region, we see a much
335   smaller seasonal amplitude in pCO_2 (15 µatm; Figure 6c), peaking in July with warming, falling to a minimum in October. The seasonal amplitude is dampened by the competing effect of temperature changes in solubility, and changes in dissolved inorganic carbon concentration through biological drawdown and changing mixed layer depth (Wong et al., 2010; Sutton et al., 2017). With minimal seasonal variation in seawater pCO_2, the seasonal change in atmospheric CO_2 uptake south of 52°N (Figure 6a) is dominantly driven by higher wind speed through the winter months (mean increase of 55% over summer
340   climatological values).

4.2 Alaskan Gyre upwelling strength

On sub-decadal to decadal timescales, there is a strong correlation between air-sea CO_2 flux anomalies and SSH anomalies in the Alaskan Gyre region of our study area ($r^2 = 0.93$, $p <0.01$; Figure 7b&c; supplementary Figure 8). In this subpolar gyre, prevailing winds cause upwelling driven by Ekman pumping (Gargett, 1991), but the strength varies. During 1998-2002 as well as 2006-2013, we observe strong winter and spring outgassing in the Alaskan Gyre, with flux densities as high as 3.6 mol m^{-2} yr^{-1} in January 2000 (Figure 7a). In these same periods, anomalously low sea level pressure over the Alaskan Gyre led to anomalously strong wind stress curl which enhanced Ekman pumping and depressed SSH (Figure 7b; Mann and Lazier 2006; Hristova et al. 2019). The stronger upwelling brought CO_2-rich subsurface water to the surface (Lagerloef et al., 1998). Conversely, during the periods of anomalously high sea level pressures and positive SSH anomalies (2003-2005; 2014-2020; Figure 7c), there is less upwelling of CO_2-rich subsurface water to the surface, allowing primary productivity to draw down surface ocean CO_2 (McKinley et al., 2006), enhancing CO_2 uptake from the atmosphere (Figure 7b).

Our observation-based findings show strong carbon relationships with SSH in the Alaskan Gyre, with correlations between other climate indices being weaker. Over longer timescales, climate-driven regional ocean fluctuations have been shown to modulate the Alaskan Gyre surface water inorganic carbon system (Hauri et al., 2021; Di Lorenzo et al., 2008). The North Pacific Gyre Oscillation and the Pacific Decadal Oscillation indices have both been shown to strongly influence the physics, chemistry, and biology of Gulf of Alaska ecosystem (Di Lorenzo et al., 2008; Newman et al., 2016). Hauri et al. (2021) showed that the rate of ocean acidification in a hindcast model of the Gulf of Alaska was strongly related to the first empirical orthogonal function of SSH. We report the same relationship with SSH described in Hauri et al. (2021) as the dominant control of sub-decadal patterns on air-sea CO_2 fluxes from our observation-based pCO$_2$ product (Figure 7). Our estimates of the 12-month running mean air-sea CO_2 flux anomaly in the Alaskan Gyre region (Figure 7b) are more weakly correlated to the North Pacific Gyre Oscillation, Pacific Decadal Oscillation, and the El Niño-Southern Oscillation indices ($r^2 = 0.63$, 0.38, 0.22 respectively; $p <0.01$). This regional variation in SSH correlating with both observations and models lends strong evidence for variations in Alaskan Gyre upwelling strength explaining regional biogeochemistry on sub-decadal to decadal timescales. This relationship supports work showing that the SSH anomaly is an important climate index for the region (Cummins et al., 2005; Di Lorenzo et al., 2008). This finding also highlights the challenges of representing the regional seasonal cycle of the Northeast Pacific in a climatology within a reference period dominated by one mode of Alaskan Gyre upwelling strength.

4.3 Impact of interannual events

On shorter, interannual timescales, basin-wide variability in air-sea CO_2 flux is significantly influenced by the impact of extreme events, with the underlaying sub-decadal and decadal signal amplifying or dampening these impacts. During persistent marine heatwaves in the Northeast Pacific since 2013, we see strong atmospheric CO_2 uptake anomalies fueled by reduced winter mixing and increased surface density stratification (Figure 8; Bond et al., 2015). The strongest marine heatwave, known as "the Blob", with sea surface temperature anomalies greater than 3°C or 4 standard deviations above normal (Freeland and

Ross, 2019), persisted in the Northeast Pacific from late 2013 to the end of 2015 driven by an anomalous high-pressure atmospheric ridge (Bond et al., 2015; Di Lorenzo and Mantua, 2016). The ridge was associated with a significant decline in

375 local wind speed, decreasing the mixing of deep, colder waters to the surface and raising sea surface temperatures (Bond et al., 2015; Scannell et al., 2020). The reduced winter mixed layer deepening and associated limiting of upwelled and entrained nutrient and CO_2-rich subsurface waters to the surface has been linked to a relief of ocean acidification (i.e., anomalously high aragonite saturation states; Mogen et al. 2022). There has also been a reported increase in net primary production during "the Blob" in both in-situ and satellite records (Long et al., 2021; Yu et al., 2019; Peña et al., 2019). During "the Blob," we see

380 strong negative air-sea CO_2 flux anomalies, particularly in the winter months (October to December 2014 and 2015), indicative of a 30% increase in uptake relative to climatological monthly means. The increased atmospheric CO_2 uptake is driven by reduced winter wind speeds (by approximately 7%) leading to limited winter mixed layer deepening, increased surface density stratification, while possibly being enhanced by the increase in net primary production (Figure 8b).

Through a second marine heatwave from mid-2018 to 2020 (Chen et al., 2021; Amaya et al., 2020; Scannell et al., 2020), we

385 see a similar magnitude increase in atmospheric CO_2 uptake compared to "the Blob" event (Figure 8b). Through some of the largest SST anomalies (October to December 2018 and 2019) we observed large negative air-sea CO_2 flux anomalies indicating enhanced atmospheric uptake of 45% beyond corresponding climatological monthly means (Figure 8b), particularly in the Alaskan Gyre (Figure 7a&b). During this marine heatwave, a similar reduction in upper ocean mixing and limited wintertime entrainment due to reduced wind speed were observed (by approximately 9%; Amaya et al., 2020) and resultant reduced

390 surface pCO_2 (Franco et al., 2021). Increased net primary production has also been reported (Long et al., 2021). An unusual near-surface freshwater anomaly in the Gulf of Alaska during 2019 contributed to the intensification of the marine heatwave by increasing the near-surface buoyancy and density stratification (Scannell et al., 2020).

Our result that marine heatwaves cause enhanced CO_2 uptake in the North Pacific subpolar gyre ~~Northeast Pacific~~ may not be applicable to a wider region. Mignot et al. (2022) described how the impact of marine heatwaves on air-sea CO_2 fluxes are the

395 net result of two competing mechanisms: 1) increased sea surface temperatures reducing the solubility of CO_2, increasing pCO_2 and reducing CO_2 uptake, and 2) increased density stratification reducing vertical mixing and entrainment, decreasing surface dissolved inorganic carbon, and increasing CO_2 uptake. Their analysis finds that the temperature effect outweighs the advection effect during persistent marine heatwaves in the ~~whole~~ North Pacific subtropical gyre ~~(from 123.5°E to 121.5°W and 23.5°N to 59.5°N; Mignot et al. 2022)~~ reducing CO_2 uptake by 29±11%, with the opposite true in the Tropical Pacific (Mignot et al.,

400 2022). However, when looking at our more localized study area in the Northeast Pacific, we find instead that the impact of reduced winter mixing (because of decreased winds and increased density stratification) tipped the balance toward enhanced atmospheric CO_2 uptake during these marine heatwaves, again advocating the need for high resolution local studies to better understand local climate change effects.

Through both "the Blob" and the 2019 marine heatwave, the Alaskan Gyre was in a period of weak upwelling (Figure 7c),

405 leading to a decade-long negative pCO_2 anomaly (Figure 8a), in addition to the maximum observed ΔpCO_2 due to the diverging long-term trend with the atmosphere (Section 4.4). Unravelling the individual influence of these interconnected drivers (i.e.,

marine heatwaves, sub-decadal variability, and long-term trend) is not possible with this product but does prompt future inquiry in combination with regional models and emerging climate analysis tools (e.g., Chapman et al., 2022).

We do not observe a large change in atmospheric CO_2 uptake associated with the 2008 basin-wide ocean iron fertilization event. In August 2008, the eruption of Kasatochi volcano in the Aleutian Islands, Alaska, USA dispersed volcanic ash over an unusually large area of the subarctic Northeast Pacific fueling a massive phytoplankton bloom in the iron-limited region (Langmann et al., 2010; Hamme et al., 2010). Hamme et al. (2010) reported that enhanced biological uptake drew down pCO_2 by approximately 25 µatm at Ocean Station Papa. Basin-wide, we see a decrease of 20 µatm from July to August 2008 in the detrended, deseasonalized ANN pCO_2 following the eruption (Figure 8a) with a drawdown of 30 µatm at Ocean Station Papa. The neural network approach does display a tendency to slightly overestimate relatively low pCO_2 values (Figure 2a). Because this basin-wide enhanced primary production and surface ocean pCO_2 decrease lasted only two months, its impact on the air-sea CO_2 flux was limited (Figure 8b). The limited impact could be tied to weaker summer wind speeds and longer equilibration times (Jones et al., 2014). The eruption occurred during a period of enhanced Alaskan Gyre upwelling (Figure 7c), meaning the event was overlaid on top of an already sub-decade long positive pCO_2 anomaly (Figure 8a) perhaps dampening the event's impact. Unfortunately, the lack of direct pCO_2 measurements in SOCAT during this time prevents us from further investigating the underlaying causes.

4.4 Air-sea CO_2 flux trend

Overall, the Northeast Pacific Ocean CO_2 sink has become more negative (i.e., become a larger sink; Figure 9b) from 1998 to 2020 at a rate of -0.043±0.004 mol m^{-2} yr^{-2}. Looking at the start and end of the timeseries, the average flux from 1998 to 2002 appeared to be a small atmospheric CO_2 sink at -0.7±0.6 mol m^{-2} yr^{-1}, compared to the sink from 2016-2020 at -1.6±0.8 mol m^{-2} yr^{-1}. Regionally, we don't see a statistically significant trend in the satellite-based ocean surface wind speed data over this time (p >0.1; Mears et al. 2019). However, the timeseries endpoints are ~~both~~ representative of different Alaskan Gyre upwelling modes (Figure 7c), with the timeseries starting in a sub-decade long positive pCO_2 anomaly and ending during a decade long negative pCO_2 anomaly. Decadal trends will be sensitive to the start and end point of the timeseries (e.g., Fay and McKinley 2013). We caution that our trend results may not be representative of longer time periods (i.e., from industrial onset).

Taking the full study area deseasonalized (Section 2.4), area-averaged pCO_2, we calculated trends based on shorter time series within our data using different monthly timeseries start and end dates (Figure 10). Based on pCO_2 data timeseries ranges greater than 10 years (between 1998 and 2020), 87% of trends are less than the atmospheric trend with a mean of 1.59±0.27 µatm yr^{-1} (N = 9222 at a monthly timestep; Figure 10). In the remaining 13% of total timeseries start and end date combinations, there is a pronounced very steep trend exceeding the atmospheric. Date combinations resulting in trends exceeding the atmospheric increase could be partly attributed to start and end dates coinciding with periods of weak and strong Alaskan Gyre upwelling, respectively. These upwelling modes induce negative and positive pCO_2 anomalies, which further amplify the observed trend. ~~Date combinations leading to trends greater than atmospheric could be partially tied to if both the start and end~~

~~dates fall within a strong Alaskan Gyre upwelling mode driving positive pCO$_2$ anomalies.~~ However, the Alaskan Gyre region

440 makes up only about 25% of the total study area (region north of 52°N; Section 4.2), and trends in Figure 10 represent the ANN-NEP full spatial domain.

The rate of change in the air-sea CO_2 flux over the study period is largely due to the increasing gradient with the atmosphere (Figure 9a). Over the full study area from 1998-2020, the ANN-NEP pCO$_2$ trend is 1.4±0.1 µatm yr^{-1}. The Landschützer et al. (2020b) global product trend in the region is similar at 1.5±0.1 µatm yr^{-1}. At Ocean Station Papa, the ANN-NEP pCO$_2$ trend

445 is 1.5±0.1 µatm yr^{-1}, in agreement with the observed trend based on discrete samples collected 1–3 times per year (1.6±0.8 µatm yr^{-1} between 1990-2019; Franco et al. 2021). The ocean pCO$_2$ trend is not as rapid as the atmospheric increase of 2.12±0.03 µatm yr^{-1} over the same period (Figure 9a). Sutton et al. (2017) also reported a lag with the atmosphere at Ocean Station Papa with a ΔpCO$_2$ trend of -1.5±0.9 µatm yr^{-1} from the 2007-2014 mooring pCO$_2$ data. The ANN-NEP ΔpCO$_2$ trend at Ocean Station Papa is -0.67±0.05 µatm yr^{-1}.

450 The observed lag in the increase in surface ocean pCO$_2$ with respect to atmospheric pCO$_2$, causing an increasing air-sea gradient (ΔpCO$_2$), may be attributed to interaction with subsurface water. We find a strong spatial correlation between the trend in ΔpCO$_2$ and the calculated average vertical velocity associated with Ekman pumping ~~calculated from zonal and meridional wind speeds~~ (r^2 = 0.64, p <0.01; Figure 11~~b; Mears et al., 2019)~~). Ekman pumping was calculated using the MATLAB Climate Toolbox ekman function (Greene et al., 2019, 2017; Kessler, 2002) from monthly, 1/4° spatial resolution

455 Cross-Calibrated Multiplatform zonal and meridional ocean surface wind speeds (Mears et al., 2019) interpolated to 1/12°. Fay and McKinley (2013) describe regions impacted by upwelling from depth having shallower pCO$_2$ trends and greater divergence with the atmosphere based on models and observations. Dissolved inorganic carbon increases with depth, causing enhanced vertical mixing to increase surface ocean pCO$_2$ over the seasonal cycle (Sections 4.1 to 4.3). However, in the long-term, dissolved inorganic carbon is increasing most in surface waters, due to direct uptake of atmospheric CO_2, and least at

460 depth. The supply to the surface of subsurface waters with low anthropogenic carbon causes a lag in the rate of increase in surface ocean pCO$_2$. The anthropogenic carbon signal in the intermediate to deep waters in this region are some of the smallest in the global ocean due to circulation patterns (Sabine et al., 2004; Gruber et al., 2019; Carter et al., 2019; Clement and Gruber, 2018). Regions within our study area with greater connection between surface and deep waters, such as the center of the Alaskan Gyre in the north (Van Scoy et al., 1991), are experiencing the largest divergence with the atmosphere. With a joint

465 increase in projected future wind speeds (Zheng et al., 2016; Young and Ribal, 2019; Wanninkhof and Triñanes, 2017), and a growing ΔpCO$_2$, the region is likely to become a stronger net annual sink for atmospheric CO_2.

5 Conclusions

Using a high-resolution regional neural network approach, we represent pCO$_2$ measurement variability well in the Northeast Pacific Ocean. We interpolated sparse observations using non-linear relationships developed with a neural network approach

based on predictor data from satellite and reanalysis products to create a continuous monthly pCO_2 estimate at 1/12°x1/12°
spatial resolution. Using a cross-evaluation ensemble approach we were able to produce a robust pCO_2 product that represents
regional variability with an uncertainty of 12 µatm. We found that stepping to a significantly higher spatial resolution,
compared to typical open ocean observation-based pCO_2 products (1/4° or 1° spatial resolution), ~~regional pCO_2 product~~ led
to nearly no loss in performance despite a much lower ratio of gridded pCO_2 observations compared to the total number of
grid cells. The most important parameter for reducing overfitting across regional pCO_2 products with different spatial
resolutions was the internal division of training data. Higher resolution products require more direct training data and less data
to internally evaluate, while still comparing to independent withheld data. This work shows that high-resolution, high-
performance, observation-based neural network derived pCO_2 products can be developed when reducing the complexity of
controlling processes by focusing on specific regions. However, chosen predictor variables need to be regionally specific
considering "process focused" influences on the local carbon system. Our reported optimization of the internal data division
ratio between network training and evaluation data indicates the importance of this choice when moving to a higher spatial
resolution. Increased spatial resolution will be necessary to capture variability in regions strongly influenced by mesoscale
processes, enabling resolution of oceanographic features such as eddies, upwelling regimes, and gyre system gradients.

We report pronounced variability in marine CO_2 uptake in the Northeast Pacific Ocean dominantly driven by the control of
Alaskan Gyre upwelling and connectivity to subsurface waters. Overall, the open ocean Northeast Pacific acted as a net sink
for atmospheric CO_2 from 1998 to 2020 with an average basin wide air-sea CO_2 flux of -1.2±1.4 mol m^{-2} yr^{-1} but with
pronounced seasonality. In the northern Alaskan Gyre region, wintertime upwelling and entrainment lead to significant
outgassing. In the southern North Pacific Current region, the seasonal flux cycle is largely driven by wind speed where the
seasonal change in surface ocean pCO_2 remains small. Based on our product, upwelling strength of the Alaskan Gyre dominates
air-sea CO_2 flux variability in that region on sub-decadal to decadal timescales. During prolonged periods of enhanced gyre
upwelling, we see strong winter outgassing driven by upwelled and entrained CO_2-rich subsurface waters. During periods of
weak gyre upwelling, the northern part of our study area acts as a sink for atmospheric CO_2 year-round. During two recent
marine heatwaves we see enhanced CO_2 uptake due to limited wintertime entrainment of subsurface waters resulting from
weaker winds. However, we observed minimal impact on atmospheric CO_2 uptake following a 2008 volcanic eruption, with
air-sea CO_2 flux anomalies linked to enhanced biological uptake via iron fertilization lasting only two months. The gradient
between the Northeast Pacific surface ocean pCO_2 and atmospheric CO_2 is increasing, pushing the region towards becoming
an enhanced sink for atmospheric CO_2. We see the largest increase in the gradient, and so potential for greater future uptake,
at the center of the Alaskan Gyre where, through upwelling, there is a strong connection with subsurface waters low in
anthropogenic CO_2.

The regional, high-resolution pCO_2 product created here could serve as a valuable baseline for regional models (e.g., Pilcher
et al., 2018; Hauri et al., 2020). The pCO_2 product, and associated air-sea CO_2 flux estimates, offers continuous coverage in
sparsely sampled regions informed by patterns in well sampled neighbouring waters. The product could be used to aid in model

505 Our analysis illustrates the complex interplay between factors driving air-sea CO_2 flux variability at varying temporal scales across the study domain and within broad subregions (Alaskan Gyre and North Pacific Current regions) allowing us to suggest what resources will be needed to make further advances. Improvement of estimated pCO_2 would benefit from an increase in the number of pCO_2 observations used for training. We recommend prioritizing additional measurements in the northern Alaskan Gyre region in future observational programs. Our estimated fluxes in the gyre are large (both uptake and outgassing),

510 but observations are sparse, leading to the largest standard deviations between our cross-evaluation ensemble members (supplementary Figure 4). The impact of sub-decadal to decadal variability on the trend in surface ocean pCO_2 and in regional atmospheric CO_2 uptake emphasises the importance of long duration timeseries sites and programs to capture the natural cycles of variability and accurately estimate change. Our findings and estimated pCO_2 product serve as environmental baselines, which could be used to inform future marine carbon dioxide removal in the Northeast Pacific at the basin and regional scale.

515 However, use of our product at the individual grid cell level is not encouraged as errors likely remain high, whereas over broader regions these errors average away. Our study serves as an important initial step in creating a complete carbon budget for the Northeast Pacific, with coastal, pelagic, and benthic carbon stocks and fluxes still to be resolved.

Code and data availability

All data used is publicly available. ANN-NEP pCO_2 and air-sea CO_2 flux fields are available through the National Center for

520 Environmental Information (NCEI Accession 0277836; https://doi.org/10.25921/c1w8-6v02). pCO_2 data are from the Surface Ocean CO_2 Atlas (SOCAT) v2021 (available at https://www.socat.info/) as well as additional data from Fisheries and Oceans Canada February 2019 Line P cruise (available at https://www.waterproperties.ca/linep/). Sea surface temperature and chlorophyll-a are from the European Space Agency Climate Change Initiative (available at https://climate.esa.int/en/odp/#/dashboard). Sea surface salinity, sea surface height, and mixed layer depth are from Copernicus

525 Marine Environment Monitoring Service (available at https://data.marine.copernicus.eu/product/GLOBAL_MULTIYEAR_PHY_001_030/description). Ocean surface wind data are from Cross-Calibrated Multiplatform version 2 Wind Vector Analysis Product (available at https://www.remss.com/measurements/ccmp/).

Author contributions

530 PD and PL developed the neural network code and created the product with help from RH, DI, NS, and MA. PD, RH, DI, and PL contributed to the interpretation and analysis of the results. All co-authors contributed to editing the manuscript. RH and

DI supervised the project work. PC provided data and consultation. PD prepared the manuscript with contributions from all co-authors.

Competing interests

535 The contact author has declared that none of the authors has any competing interests.

Disclaimer

This article reflects only the authors' view – the funding agencies as well as their executive agencies are not responsible for any use that may be made of the information that the article contains.

Acknowledgement

540 Ocean Station Papa mooring timeseries site, plus the Line P program are operated by the National Oceanic and Atmospheric Administration and Fisheries and Oceans Canada.

Financial support

Funding for this project was provided by the Natural Sciences and Engineering Research Council of Canada (NSERC) through the Advancing Climate Change Science in Canada program (grant# ACCPJ 536173-18) to RH. Funding from Fisheries and
545 Oceans Canada's Aquatic Climate Change Adaptation Service Program to PC supported the analysis of recent underway pCO_2 measurements made by the Line-P program (grant# 96036). PD financial support also provided by a Natural Sciences and Engineering Research Council of Canada (NSERC) Doctoral Postgraduate Scholarship.

References

Amari, S., Murata, N., Müller, K.-R., Finke, M., and Yang, H. H.: Asymptotic Statistical Theory of Overtraining and Cross-
550 Validation, IEEE T. Neural Network, 8, 985–996, 1997.

Amaya, D. J., Miller, A. J., Xie, S. P., and Kosaka, Y.: Physical drivers of the summer 2019 North Pacific marine heatwave, Nature Communications, 11, 1–9, https://doi.org/10.1038/s41467-020-15820-w, 2020.

Aricò, S., Arrieta, J. M., Bakker, D. C. E., Boyd, P. W., Cotrim da Cunha, L., Chai, F., Dai, M., Gruber, N., Isensee, K., Ishii, M., Jiao, N., Lauvset, S. K., McKinley, G. A., Monteiro, P., Robinson, C., Sabine, C., Sanders, R., Schoo, K. L., Schuster, U.,
555 Shutler, J. D., Thomas, H., Wanninkhof, R., Watson, A. J., Bopp, L., Boss, E., Bracco, A., Cai, W., Fay, A., Feely, R. A., Gregor, L., Hauck, J., Heinze, C., Henson, S., Hwang, J., Post, J., Suntharalingam, P., Telszewski, M., Tilbrook, B., Valsala, V., and ojas Aldana, A.: Integrated Ocean Carbon Research: A Summary of Ocean Carbon Research, and Vision of Coordinated Ocean Carbon Research and Observations for the Next Decade, 46, https://doi.org/10.25607/h0gj-pq41, 2021.

Aumont, O., Maier-Reimer, E., Blain, S., and Monfray, P.: An ecosystem model of the global ocean including Fe, Si, P colimitations, Global Biogeochemical Cycles, 17, https://doi.org/10.1029/2001gb001745, 2003.

Bakker, D. C. E., Pfeil, B., Landa, C. S., Metzl, N., O'Brien, K. M., Olsen, A., Smith, K., Cosca, C., Harasawa, S., Jones, S. D., Nakaoka, S. I., Nojiri, Y., Schuster, U., Steinhoff, T., Sweeney, C., Takahashi, T., Tilbrook, B., Wada, C., Wanninkhof, R., Alin, S. R., Balestrini, C. F., Barbero, L., Bates, N. R., Bianchi, A. A., Bonou, F., Boutin, J., Bozec, Y., Burger, E. F., Cai, W. J., Castle, R. D., Chen, L., Chierici, M., Currie, K., Evans, W., Featherstone, C., Feely, R. A., Fransson, A., Goyet, C., Greenwood, N., Gregor, L., Hankin, S., Hardman-Mountford, N. J., Harlay, J., Hauck, J., Hoppema, M., Humphreys, M. P., Hunt, C. W., Huss, B., Ibánhez, J. S. P., Johannessen, T., Keeling, R., Kitidis, V., Körtzinger, A., Kozyr, A., Krasakopoulou, E., Kuwata, A., Landschützer, P., Lauvset, S. K., Lefèvre, N., Lo Monaco, C., Manke, A., Mathis, J. T., Merlivat, L., Millero, F. J., Monteiro, P. M. S., Munro, D. R., Murata, A., Newberger, T., Omar, A. M., Ono, T., Paterson, K., Pearce, D., Pierrot, D., Robbins, L. L., Saito, S., Salisbury, J., Schlitzer, R., Schneider, B., Schweitzer, R., Sieger, R., Skjelvan, I., Sullivan, K. F., Sutherland, S. C., Sutton, A. J., Tadokoro, K., Telszewski, M., Tuma, M., Van Heuven, S. M. A. C., Vandemark, D., Ward, B., Watson, A. J., and Xu, S.: A multi-decade record of high-quality fCO_2 data in version 3 of the Surface Ocean CO_2 Atlas (SOCAT), Earth System Science Data, 8, 383–413, https://doi.org/10.5194/essd-8-383-2016, 2016.

Bond, N. A., Cronin, M. F., Freeland, H., and Mantua, N.: Causes and impacts of the 2014 warm anomaly in the NE Pacific, Geophysical Research Letters, 42, 3414–3420, https://doi.org/10.1002/2015GL063306, 2015.

Boyd, P. W., Strzepek, R., Jackson, G., Wong, C. S., Mckay, R. M., Law, C., Sherry, N., Johnson, K., and Gower, J.: The evolution and termination of an iron-induced mesoscale bloom in the northeast subarctic Pacific, Limnology and Oceanography, 50, 1872–1886, https://doi.org/10.4319/lo.2005.50.6.1872, 2005.

Boyd, P. W., Jickells, T., Law, C. S., Blain, S., Boyle, E. A., Buesseler, K. O., Coale, K. H., Cullen, J. J., Baar, H. J. W. D., Follows, M., Harvey, M., Lancelot, C., and Levasseur, M.: Mesoscale Iron Enrichment Experiments 1993 – 2005: Synthesis and Future Directions, Science, 315, 612–618, https://doi.org/10.1126/science.1131669, 2007.

Brady, R. X., Lovenduski, N. S., Alexander, M. A., Jacox, M., and Gruber, N.: On the role of climate modes in modulating the air-sea CO_2 fluxes in eastern boundary upwelling systems, Biogeosciences, 16, 329–346, https://doi.org/10.5194/bg-16-329-2019, 2019.

Carter, B. R., Feely, R. A., Wanninkhof, R., Kouketsu, S., Sonnerup, R. E., Pardo, P. C., Sabine, C. L., Johnson, G. C., Sloyan, B. M., Murata, A., Mecking, S., Tilbrook, B., Speer, K., Talley, L. D., Millero, F. J., Wijffels, S. E., Macdonald, A. M., Gruber, N., and Bullister, J. L.: Pacific Anthropogenic Carbon Between 1991 and 2017, Global Biogeochemical Cycles, 33, 597–617, https://doi.org/10.1029/2018GB006154, 2019.

Chapman, C. C., Monselesan, D. P., Risbey, J. S., Feng, M., and Sloyan, B. M.: A large-scale view of marine heatwaves revealed by archetype analysis, Nat Commun, 13, 7843, https://doi.org/10.1038/s41467-022-35493-x, 2022.

Chen, S., Hu, C., Byrne, R. H., Robbins, L. L., and Yang, B.: Remote estimation of surface pCO_2 on the West Florida Shelf, Continental Shelf Research, 128, 10–25, https://doi.org/10.1016/j.csr.2016.09.004, 2016.

Chen, S., Hu, C., Barnes, B. B., Wanninkhof, R., Cai, W. J., Barbero, L., and Pierrot, D.: A machine learning approach to estimate surface ocean pCO_2 from satellite measurements, Remote Sensing of Environment, 228, 203–226, https://doi.org/10.1016/j.rse.2019.04.019, 2019.

Chen, Z., Shi, J., Liu, Q., Chen, H., and Li, C.: A Persistent and Intense Marine Heatwave in the Northeast Pacific During 2019–2020, Geophysical Research Letters, 48, 1–9, https://doi.org/10.1029/2021GL093239, 2021.

Chierici, M., Fransson, A., and Nojiri, Y.: Biogeochemical processes as drivers of surface fCO2 in contrasting provinces in the subarctic North Pacific Ocean, Global Biogeochemical Cycles, 20, 1–16, https://doi.org/10.1029/2004GB002356, 2006.

Clement, D. and Gruber, N.: The eMLR (C *) Method to Determine Decadal Changes in the Global Ocean Storage of
600 Anthropogenic CO 2, 654–679, https://doi.org/10.1002/2017GB005819, 2018.

Cooley, S. R., Klinsky, S., and Morrow, D. R.: Sociotechnical Considerations About Ocean Carbon Dioxide Removal, Annual Review of Marine Science, 15, 1–26, https://doi.org/10.1146/annurev-marine-032122-113850, 2022.

Cummins, P. F., Lagerloef, G. S. E., and Mitchum, G.: A regional index of northeast Pacific variability based on satellite altimeter data, Geophysical Research Letters, 32, https://doi.org/10.1029/2005GL023642, 2005.

605 Denvil-Sommer, A., Gehlen, M., Vrac, M., and Mejia, C.: LSCE-FFNN-v1: A two-step neural network model for the reconstruction of surface ocean pCO2 over the global ocean, Geoscientific Model Development, 12, 2091–2105, https://doi.org/10.5194/gmd-12-2091-2019, 2019.

Di Lorenzo, E. and Mantua, N.: Multi-year persistence of the 2014/15 North Pacific marine heatwave, Nature Climate Change, 6, 1042–1047, https://doi.org/10.1038/nclimate3082, 2016.

610 Di Lorenzo, E., Schneider, N., Cobb, K. M., Franks, P. J. S., Chhak, K., Miller, A. J., McWilliams, J. C., Bograd, S. J., Arango, H., Curchitser, E., Powell, T. M., and Rivière, P.: North Pacific Gyre Oscillation links ocean climate and ecosystem change, Geophysical Research Letters, 35, 2–7, https://doi.org/10.1029/2007GL032838, 2008.

Dickson, A. G., Sabine, C. L., and Christian, J. R.: Guide to Best Practices for Ocean CO2 Measurements, 191 pp., 2007.

Dugdale, R. C. and Wilkerson, F. P.: Low Specific Nitrate Uptake Rate: A Common Feature of High-Nutrient, Low-
615 Chlorophyll Marine Ecosystems, Limnology and oceanography, 36, 1678–1688, https://doi.org/10.4319/lo.1991.36.8.1678, 1991.

Duke, P. J., Hamme, R. C., Ianson, D., Landschützer, P., Ahmed, M. M. M., Swart, N. C., and Covert, P. A.: ANN-NEP: A monthly surface pCO2 product for the Northeast Pacific open ocean from 1998-01-01 to 2019-12-31 (NCEI Accession 0277836), https://doi.org/10.25921/c1w8-6v02, 2023a.

620 Duke, P. J., Richaud, B., Arruda, R., Länger, J., Schuler, K., Gooya, P., Ahmed, M. M. M., Miller, M. R., Braybrook, C. A., Kam, K., Piunno, R., Sezginer, Y., Nickoloff, G., and Franco, A. C.: Canada's marine carbon sink: an early career perspective on the state of research and existing knowledge gaps, FACETS, 8, 1–21, https://doi.org/10.1139/facets-2022-0214, 2023b.

Fay, A. R. and McKinley, G. A.: Global trends in surface ocean pCO2 from in situ data, Global Biogeochemical Cycles, 27, 541–557, https://doi.org/10.1002/gbc.20051, 2013.

625 Fay, A. R., Gregor, L., Landschützer, P., McKinley, G. A., Gruber, N., Gehlen, M., Iida, Y., Laruelle, G. G., Rödenbeck, C., Roobaert, A., and Zeng, J.: SeaFlux: Harmonization of air-sea CO2 fluxes from surface pCO2 data products using a standardized approach, Earth System Science Data, 13, 4693–4710, https://doi.org/10.5194/essd-13-4693-2021, 2021.

Fourrier, M., Coppola, L., Claustre, H., D'Ortenzio, F., Sauzède, R., and Gattuso, J. P.: A Regional Neural Network Approach to Estimate Water-Column Nutrient Concentrations and Carbonate System Variables in the Mediterranean Sea: CANYON-
630 MED, Frontiers in Marine Science, 7, 1–20, https://doi.org/10.3389/fmars.2020.00620, 2020.

Franco, A. C., Ianson, D., Ross, T., Hamme, R. C., Monahan, A. H., Christian, J. R., Davelaar, M., Johnson, W. K., Miller, L. A., Robert, M., and Tortell, P. D.: Anthropogenic and climatic contributions to observed carbon system trends in the Northeast Pacific, Global Biogeochemical Cycles, 1–21, https://doi.org/10.1029/2020gb006829, 2021.

Freeland, H.: A short history of Ocean Station Papa and Line P, Progress in Oceanography, 75, 120–125, https://doi.org/10.1016/j.pocean.2007.08.005, 2007.

Freeland, H. and Ross, T.: 'The Blob' - or, how unusual were ocean temperatures in the Northeast Pacific during 2014-2018?, Deep-Sea Research Part I: Oceanographic Research Papers, 150, 103061, https://doi.org/10.1016/j.dsr.2019.06.007, 2019.

Freeland, H. J., Crawford, W. R., and Thomson, R. E.: Currents along the pacific coast of canada, Atmosphere - Ocean, 22, 151–172, https://doi.org/10.1080/07055900.1984.9649191, 1984.

Friedlingstein, P., Sullivan, M. O., Jones, M. W., Andrew, R. M., Gregor, L., Hauck, J., Quéré, C. L., Luijkx, I. T., Olsen, A., Peters, G. P., and Peters, W.: Global Carbon Budget 2022, Earth System Science Data, 14, 4811–4900, https://doi.org/10.5194/essd-14-4811-2022, 2022.

Frölicher, T. L., Fischer, E. M., and Gruber, N.: Marine heatwaves under global warming, Nature, 560, 360–364, https://doi.org/10.1038/s41586-018-0383-9, 2018.

Gargett, A. E.: Physical processes and the maintenance of nutrient-rich euphotic zones, Limnology and Oceanography, 36, 1527–1545, https://doi.org/10.4319/lo.1991.36.8.1527, 1991.

GESAMP: High level review of a wide range of proposed marine geoengineering techniques, GESAMP Reports and Studies, Joint Group of Experts on the Scientific Aspects of Marine Environmental Protections, 2019.

Global Ocean Surface Carbon, E.U. Copernicus Marine Service Information MULTIOBS_GLO_BIO_CARBON_SURFACE_REP_015_008:

Global Ocean Physical Reanalysis Product, E.U. Copernicus Marine Service Information GLOBAL_REANALYSIS_PHY_001_030:

ESA Sea Surface Temperature Climate Change Initiative (SST_cci): Level 4 Analysis Climate Data Record, version 2.1:

Greene, C. A., Blankenship, D. D., Gwyther, D. E., Silvano, A., and van Wijk, E.: Wind causes Totten Ice Shelf melt and acceleration, Science Advances, 3, e1701681, https://doi.org/10.1126/sciadv.1701681, 2017.

Greene, C. A., Thirumalai, K., Kearney, K. A., Delgado, J. M., Schwanghart, W., Wolfenbarger, N. S., Thyng, K. M., Gwyther, D. E., Gardner, A. S., and Blankenship, D. D.: The Climate Data Toolbox for MATLAB, Geochemistry, Geophysics, Geosystems, 20, 3774–3781, https://doi.org/10.1029/2019GC008392, 2019.

Gregor, L., Kok, S., and Monteiro, P. M. S.: Interannual drivers of the seasonal cycle of CO2 in the Southern Ocean, Biogeosciences, 15, 2361–2378, https://doi.org/10.5194/bg-15-2361-2018, 2018.

Gruber, N., Clement, D., Carter, B. R., Feely, R. A., van Heuven, S., Hoppema, M., Ishii, M., Key, R. M., Kozyr, A., Lauvset, S. K., Monaco, C. L., Mathis, J. T., Murata, A., Olsen, A., Perez, F. F., Sabine, C. L., Tanhua, T., and Wanninkhof, R.: The oceanic sink for anthropogenic CO2 from 1994 to 2007, Science, 363, 1193–1199, https://doi.org/10.1126/science.aau5153, 2019.

Gruber, N., Bakker, D. C. E., Devries, T., Gregor, L., Hauck, J., Landschützer, P., Mckinley, G. A., and Müller, J. D.: Trends and variability in the ocean carbon sink, Nature Reviews Earth & Environment, 1–16, https://doi.org/10.1038/s43017-022-00381-x, 2023.

Hales, B., Strutton, P. G., Saraceno, M., Letelier, R., Takahashi, T., Feely, R., Sabine, C., and Chavez, F.: Satellite-based prediction of pCO_2 in coastal waters of the eastern North Pacific, Progress in Oceanography, 103, 1–15, https://doi.org/10.1016/j.pocean.2012.03.001, 2012.

Hamme, R. C., Webley, P. W., Crawford, W. R., Whitney, F. A., Degrandpre, M. D., Emerson, S. R., Eriksen, C. C., Giesbrecht, K. E., Gower, J. F. R., Kavanaugh, M. T., Pea, M. A., Sabine, C. L., Batten, S. D., Coogan, L. A., Grundle, D. S., and Lockwood, D.: Volcanic ash fuels anomalous plankton bloom in subarctic northeast Pacific, Geophysical Research Letters, 37, 1–5, https://doi.org/10.1029/2010GL044629, 2010.

Harrison, P. J., Boyd, P. W., Varela, D. E., Takeda, S., Shiomoto, A., and Odate, T.: Comparison of factors controlling phytoplankton productivity in the NE and NW subarctic Pacific gyres, Progress in Oceanography, 43, 205–234, https://doi.org/10.1016/S0079-6611(99)00015-4, 1999.

Hauck, J., Zeising, M., Le Quéré, C., Gruber, N., Bakker, D. C. E., Bopp, L., Chau, T. T. T., Gürses, Ö., Ilyina, T., Landschützer, P., Lenton, A., Resplandy, L., Rödenbeck, C., Schwinger, J., and Séférian, R.: Consistency and Challenges in the Ocean Carbon Sink Estimate for the Global Carbon Budget, Frontiers in Marine Science, 7, 1–22, https://doi.org/10.3389/fmars.2020.571720, 2020.

Hauri, C., Schultz, C., Hedstrom, K., Danielson, S., Irving, B., C. Doney, S., Dussin, R., N. Curchitser, E., F. Hill, D., and A. Stock, C.: A regional hindcast model simulating ecosystem dynamics, inorganic carbon chemistry, and ocean acidification in the Gulf of Alaska, Biogeosciences, 17, 3837–3857, https://doi.org/10.5194/bg-17-3837-2020, 2020.

Hauri, C., Pagès, R., McDonnell, A. M. P., Stuecker, M. F., Danielson, S. L., Hedstrom, K., Irving, B., Schultz, C., and Doney, S. C.: Modulation of ocean acidification by decadal climate variability in the Gulf of Alaska, Communications Earth & Environment, 2, 1–7, https://doi.org/10.1038/s43247-021-00254-z, 2021.

Hristova, H. G., Ladd, C., and Stabeno, P. J.: Variability and Trends of the Alaska Gyre From Argo and Satellite Altimetry, Journal of Geophysical Research: Oceans, 124, 5870–5887, https://doi.org/10.1029/2019JC015231, 2019.

Hsieh, W. W.: Machine Learning Methods in the Environmental Sciences: Neural Networks and Kernels, Cambridge University Press, Vancouver, BC, Canada, 364 pp., 2009.

Ianson, D., Völker, C., Denman, K. L., Kunze, E., and Steiner, N.: The effect of vertical and horizontal dilution on fertilized patch experiments, Global Biogeochemical Cycles, 26, 1–14, https://doi.org/10.1029/2010GB004008, 2012.

Jackson, J. M., Myers, P. G., and Ianson, D.: An examination of mixed layer sensitivity in the northeast Pacific Ocean from July 2001–July 2005 using the general ocean turbulence model and Argo data, Atmosphere-Ocean, 47, 139–153, https://doi.org/10.3137/OC308.2009, 2009.

Jean-Michel, L., Eric, G., Romain, B.-B., Gilles, G., Angélique, M., Marie, D., Clément, B., Mathieu, H., and Lea, D. J.: The Copernicus Global 1 / 12 ° Oceanic and Sea Ice GLORYS12 Reanalysis, Frontiers in Earth Science, 9, 1–27, https://doi.org/10.3389/feart.2021.698876, 2021.

Jones, D. C., Ito, T., Takano, Y., and Hsu, W.: Spatial and seasonal variability of the air-sea equilibration timescale of carbon dioxide, Global Biogeochemical Cycles, 28, 1163–1178, https://doi.org/10.1002/2014GB004813, 2014.

Kalnay, E., Kanamitsu, M., Kistler, R., Collins, W., Deaven, D., Gandin, L., Iredell, M., Saha, S., White, G., Woollen, J., Zhu, Y., Chelliah, M., Ebisuzaki, W., Higgins, W., Janowiak, J., Mo, K. C., Ropelewski, C., Wang, J., Leetmaa, A., Reynolds, R., Jenne, R., and Joseph, D.: The NCEP/NCAR 40-Year Reanalysis Project, Bulletin of the American Meteorological Society, 77, 437–472, https://doi.org/10.1175/1520-0477(1996)077<0437:TNYRP>2.0.CO;2, 1996.

Keppler, L., Landschützer, P., Gruber, N., Lauvset, S. K., and Stemmler, I.: Seasonal Carbon Dynamics in the Near-Global Ocean, Global Biogeochemical Cycles, 34, e2020GB006571, https://doi.org/10.1029/2020GB006571, 2020.

Kessler, W. S.: Mean Three-Dimensional Circulation in the Northeast Tropical Pacific, Journal of Physical Oceanography, 32, 2457–2471, https://doi.org/10.1175/1520-0485(2002)032<2457:MTDCIT>2.0.CO;2, 2002.

Körtzinger, A.: Determination of carbon dioxide partial pressure (pCO2), in: Methods of Seawater Analysis, Verlag Chemie, 149–158, 1999.

Lagerloef, G. S. E., Lukas, R., Weller, R. A., and Anderson, S. P.: Pacific warm pool temperature regulation during TOGA COARE: Upper ocean feedback, Journal of Climate, 11, 2297–2309, https://doi.org/10.1175/1520-0442(1998)011<2297:PWPTRD>2.0.CO;2, 1998.

Landschützer, P., Gruber, N., Bakker, D. C. E., Schuster, U., Nakaoka, S., Payne, M. R., Sasse, T. P., and Zeng, J.: A neural network-based estimate of the seasonal to inter-annual variability of the Atlantic Ocean carbon sink, Biogeosciences, 10, 7793–7815, https://doi.org/10.5194/bg-10-7793-2013, 2013.

Landschützer, P., Gruber, N., D.C.E.Bakker, and Schuster, U.: Recent variability of the global ocean carbon sink, Global Biogeochemical Cycles, 28, 927–949, https://doi.org/10.1002/2014GB004853, 2014.

Landschützer, P., Gruber, N., Haumann, F. A., Rödenbeck, C., Bakker, D. C. E., Heuven, S. V., Hoppema, M., Metzl, N., Sweeney, C., and Takahashi, T.: The reinvigoration of the Southern Ocean carbon sink, Science, 349, 1221–1224, https://doi.org/10.1126/science.aab2620, 2015.

Landschützer, P., Gruber, N., and Bakker, D. C. E.: Decadal variations and trends of the global ocean carbon sink, Global Biogeochemical Cycles, 30, 1396–1417, https://doi.org/10.1002/2015GB005359, 2016.

Landschützer, P., Gruber, N., Bakker, D. C. E., Stemmler, I., and Six, K. D.: Strengthening seasonal marine CO2 variations due to increasing atmospheric CO2, Nature Climate Change, 8, 146–150, https://doi.org/10.1038/s41558-017-0057-x, 2018.

Landschützer, P., Ilyina, T., and Lovenduski, N. S.: Detecting Regional Modes of Variability in Observation-Based Surface Ocean pCO2, Geophysical Research Letters, 46, 2670–2679, https://doi.org/10.1029/2018GL081756, 2019.

Landschützer, P., Laruelle, G. G., Roobaert, A., and Regnier, P.: A uniform pCO2 climatology combining open and coastal oceans, Earth System Science Data, 12, 2537–2553, https://doi.org/10.5194/essd-12-2537-2020, 2020a.

Landschützer, P., Gruber, N., and Bakker, D. C. E.: An observation-based global monthly gridded sea surface pCO2 and air-sea CO2 flux product from 1982 onward and its monthly climatology, NCEI Accession, 160558, https://doi.org/10.7289/v5z899n6, 2020b.

Langmann, B., Zakšek, K., Hort, M., and Duggen, S.: Volcanic ash as fertiliser for the surface ocean, Atmospheric Chemistry and Physics, 10, 3891–3899, https://doi.org/10.5194/acp-10-3891-2010, 2010.

Laruelle, G. G., Landschützer, P., Gruber, N., Tison, J.-L., Delille, B., and Regnier, P.: Global high-resolution monthly pCO2 climatology for the coastal ocean derived from neural network interpolation, Biogeosciences Discussions, 1–40, https://doi.org/10.5194/bg-2017-64, 2017.

Li, X., Bellerby, R., Ge, J., Wallhead, P., Liu, J., and Yang, A.: Retrieving monthly and interannual total-scale pH on the East China Sea shelf using an artificial neural network: ANN-pH-v1, Geoscientific Model Development Discussions, 1–15, https://doi.org/10.5194/gmd-2019-236, 2019.

Li, X., Bellerby, R. G. J., Wallhead, P., Ge, J., Liu, J., Liu, J., and Yang, A.: A Neural Network-Based Analysis of the Seasonal Variability of Surface Total Alkalinity on the East China Sea Shelf, Frontiers in Marine Science, 7, https://doi.org/10.3389/fmars.2020.00219, 2020.

Linares-Rodriguez, A., Ruiz-Arias, J. A., Pozo-Vazquez, D., and Tovar-Pescador, J.: An artificial neural network ensemble model for estimating global solar radiation from Meteosat satellite images, Energy, 61, 636–645, https://doi.org/10.1016/j.energy.2013.09.008, 2013.

Long, J. S., Fassbender, A. J., and Estapa, M. L.: Depth-Resolved Net Primary Production in the Northeast Pacific Ocean: A Comparison of Satellite and Profiling Float Estimates in the Context of Two Marine Heatwaves, Geophysical Research Letters, 48, 1–11, https://doi.org/10.1029/2021GL093462, 2021.

Mann, K. H. and Lazier, J. R.: Dynamics of Marine Ecosystems: Biological- Physical Interactions in the Oceans, Blackwell Publishing, 2006.

Martin, J., KH, C., KS, J., SE, F., RM, G., SJ, T., CN, H., VA, E., JL, N., and TL, C.: Testing the iron hypothesis in ecosystems of the equatorial Pacific Ocean, Nature, 371, 123–129, https://doi.org/10.1038/371123a0, 1994.

McKinley, G. A., Takahashi, T., Buitenhuis, E., Chai, F., Christian, J. R., Doney, S. C., Jiang, M. S., Lindsay, K., Moore, J. K., Le Quéré, C., Lima, I., Murtugudde, R., Shi, L., and Wetzel, P.: North Pacific carbon cycle response to climate variability on seasonal to decadal timescales, Journal of Geophysical Research: Oceans, 111, https://doi.org/10.1029/2005JC003173, 2006.

McKinley, G. A., Fay, A. R., Takahashi, T., and Metzl, N.: Convergence of atmospheric and North Atlantic carbon dioxide trends on multidecadal timescales, Nature Geoscience, 4, https://doi.org/10.1038/ngeo1193, 2011.

Mears, C. A., Scott, J., Wentz, F. J., Ricciardulli, L., Leidner, S. M., Hoffman, R., and Atlas, R.: A Near-Real-Time Version of the Cross-Calibrated Multiplatform (CCMP) Ocean Surface Wind Velocity Data Set, Journal of Geophysical Research: Oceans, 124, 6997–7010, https://doi.org/10.1029/2019JC015367, 2019.

Merchant, C. J., Embury, O., Bulgin, C. E., Block, T., Corlett, G. K., Fiedler, E., Good, S. A., Mittaz, J., Rayner, N. A., Berry, D., Eastwood, S., Taylor, M., Tsushima, Y., Waterfall, A., Wilson, R., and Donlon, C.: Satellite-based time-series of sea-surface temperature since 1981 for climate applications, Scientific Data, 6, 1–18, https://doi.org/10.1038/s41597-019-0236-x, 2019.

Mignot, A., Schuckmann, K. V., Landschützer, P., Gasparin, F., Gennip, S. V., Perruche, C., Lamouroux, J., and Amm, T.: Decrease in air-sea CO 2 fluxes caused by persistent marine heatwaves, Nature Communications, 13, 1–9, https://doi.org/10.1038/s41467-022-31983-0, 2022.

Mogen, S., Lovenduski, N. S., Dallman, A. R., Gregor, L., Sutton, A. J., Bograd, S. J., Cordero Quiros, N., Di Lorenzo, E., Hazen, E. L., Jacox, M. G., and et al.: Ocean biogeochemical signatures of the North Pacific Blob, Earth and Space Science Open Archive, 49, e2021GL096938, https://doi.org/10.1029/2021GL096938, 2022.

Nakaoka, S., Telszewski, M., Nojiri, Y., Yasunaka, S., Miyazaki, C., Mukai, H., and Usui, N.: Estimating temporal and spatial variation of ocean surface pCO2 in the North Pacific using a self-organizing map neural network technique, Biogeosciences, 10, 6093–6106, https://doi.org/10.5194/bg-10-6093-2013, 2013.

NASEM: A Research Strategy for Ocean-based Carbon Dioxide Removal and Sequestration, A Research Strategy for Ocean-based Carbon Dioxide Removal and Sequestration, National Academies of Sciences, Engineering, and Medicine, Washington, DC, https://doi.org/10.17226/26278, 2021.

Newman, M., Alexander, M. A., Ault, T. R., Cobb, K. M., Deser, C., Di Lorenzo, E., Mantua, N. J., Miller, A. J., Minobe, S., Nakamura, H., Schneider, N., Vimont, D. J., Phillips, A. S., Scott, J. D., and Smith, C. A.: The Pacific decadal oscillation, revisited, Journal of Climate, 29, 4399–4427, https://doi.org/10.1175/JCLI-D-15-0508.1, 2016.

Olivier, L., Boutin, J., Reverdin, G., Lefèvre, N., Landschützer, P., Speich, S., Karstensen, J., Labaste, M., Noisel, C., Ritschel, M., and Steinhoff, T.: Wintertime process study of the North Brazil Current rings reveals the region as a larger sink for CO 2 than expected, Biogeosciences, 19, 2969–2988, https://doi.org/10.5194/bg-19-2969-2022, 2022.

O'Neill, B. C., Tebaldi, C., Vuuren, D. P. V., Eyring, V., Friedlingstein, P., Hurtt, G., Knutti, R., Kriegler, E., Lamarque, J., Lowe, J., Meehl, G. A., and Moss, R.: The Scenario Model Intercomparison Project (ScenarioMIP) for CMIP6, 3461–3482, https://doi.org/10.5194/gmd-9-3461-2016, 2018.

Palevsky, H. I., Ribalet, F., Swalwell, J. E., Cosca, C. E., Cokelet, E. D., Feely, R. A., Armbrust, E. V., and Quay, P. D.: The influence of net community production and phytoplankton community structure on CO2 uptake in the Gulf of Alaska, 664–676 pp., https://doi.org/10.1002/gbc.20058, 2013.

Parard, G., Charantonis, A. A., and Rutgerson, A.: Remote sensing the sea surface CO2 of the Baltic Sea using the SOMLO methodology, Biogeosciences, 12, 3369–3384, https://doi.org/10.5194/bg-12-3369-2015, 2015.

Parard, G., Charantonis, A. A., and Rutgersson, A.: Using satellite data to estimate partial pressure of CO2 in the Baltic Sea, Journal of Geophysical Research G: Biogeosciences, 121, 1002–1015, https://doi.org/10.1002/2015JG003064, 2016.

Peña, M. A., Nemcek, N., and Robert, M.: Phytoplankton responses to the 2014–2016 warming anomaly in the northeast subarctic Pacific Ocean, Limnology and Oceanography, 64, 515–525, https://doi.org/10.1002/lno.11056, 2019.

Pilcher, D. J., Siedlecki, S. A., Hermann, A. J., Coyle, K. O., Mathis, J. T., and Evans, W.: Simulated Impact of Glacial Runoff on CO2 Uptake in the Gulf of Alaska, Geophysical Research Letters, 45, 880–890, https://doi.org/10.1002/2017GL075910, 2018.

Reynolds, R. W., Rayner, N. A., Smith, T. M., Stokes, D. C., and Wang, W.: An Improved In Situ and Satellite SST Analysis for Climate, Journal of Climate, 15, 1609–1625, https://doi.org/10.1175/1520-0442(2002)015<1609:AIISAS>2.0.CO;2, 2002.

Ritter, R., Landschützer, P., Gruber, N., Fay, A. R., Iida, Y., Jones, S., Nakaoka, S., Park, G. H., Peylin, P., Rödenbeck, C., Rodgers, K. B., Shutler, J. D., and Zeng, J.: Observation-Based Trends of the Southern Ocean Carbon Sink, Geophysical Research Letters, 44, 12,339-12,348, https://doi.org/10.1002/2017GL074837, 2017.

Roobaert, A., Laruelle, G. G., Landschützer, P., Gruber, N., Chou, L., and Regnier, P.: The Spatiotemporal Dynamics of the Sources and Sinks of CO2 in the Global Coastal Ocean, Global Biogeochemical Cycles, 33, 1693–1714, https://doi.org/10.1029/2019GB006239, 2019.

Roobaert, A., Regnier, P., Landschützer, P., and Laruelle, G. G.: A novel sea surface pCO₂-product for the global coastal ocean
810 resolving trends over the 1982–2020 period, Earth System Science Data Discussions, 1–32,
https://doi.org/10.5194/essd-2023-228, 2023.

Rosenthal, P. B.: Testing the validity of single-particle maps at low and high resolution, Methods in enzymology, 579, 227–
253, https://doi.org/10.1016/bs.mie.2016.06.004, 2016.

Sabine, C. L., Feely, R. A., Gruber, N., Key, R. M., Lee, K., Bullister, J. L., Wanninkhof, R., Wong, C. S., Wallace, D. W. R.,
815 Tilbrook, B., Millero, F. J., Peng, T., and Kozyr, A.: The Oceanic Sink for Anthropogenic CO 2, Science, 305, 367–372,
https://doi.org/10.1126/science.1097403, 2004.

Sarmiento, J. L. and Gruber, N.: Ocean Biogeochemical Dynamics, Princeton University Press, Princeton, 1–503 pp., 2006.

ESA Ocean Colour Climate Change Initiative (Ocean_Colour_cci): Global chlorophyll-a data products gridded on a
geographic projection, Version 5.0: https://catalogue.ceda.ac.uk/uuid/e9f82908fd9c48138b31e5cfaa6d692b.

820 Scannell, H. A., Johnson, G. C., Thompson, L., Lyman, J. M., and Riser, S. C.: Subsurface Evolution and Persistence of Marine
Heatwaves in the Northeast Pacific, Geophysical Research Letters, 47, 1–10, https://doi.org/10.1029/2020GL090548, 2020.

Sharkey, A. J. C.: Combining Artificial Neural Nets: Ensemble and Modular Multi-Net Systems, Springer, Berlin, 1999.

Sharp, J. D., Fassbender, A. J., Carter, B. R., Lavin, P. D., and Sutton, A. J.: A monthly surface pCO2product for the California
Current Large Marine Ecosystem, Earth System Science Data, 14, 2081–2108, https://doi.org/10.5194/essd-14-2081-2022,
825 2022.

Sutton, A. J., Wanninkhof, R., Sabine, C. L., Feely, R. A., Cronin, M. F., and Weller, R. A.: Variability and trends in surface
seawater pCO 2 and CO 2 flux in the Pacific Ocean, Geophysical Research Letters, 44, 5627–5636,
https://doi.org/10.1002/2017GL073814, 2017.

Sutton, A. J., Feely, R. A., Maenner-Jones, S., Musielwicz, S., Osborne, J., Dietrich, C., Monacci, N., Cross, J., Bott, R.,
830 Kozyr, A., Andersson, A. J., Bates, N. R., Cai, W. J., Cronin, M. F., De Carlo, E. H., Hales, B., Howden, S. D., Lee, C. M.,
Manzello, D. P., McPhaden, M. J., Meléndez, M., Mickett, J. B., Newton, J. A., Noakes, S. E., Noh, J. H., Olafsdottir, S. R.,
Salisbury, J. E., Send, U., Trull, T. W., Vandemark, D. C., and Weller, R. A.: Autonomous seawater pCO 2 and pH time series
from 40 surface buoys and the emergence of anthropogenic trends, Earth System Science Data, 11, 421–439,
https://doi.org/10.5194/essd-11-421-2019, 2019.

835 Takahashi, T., Olafsson, J., Goddard, J. G., Chipman, D. W., and Sutherland, S. C.: Seasonal variation of CO2 and nutrients
in the high-latitude surface oceans: A comparative study, Global Biogeochemical Cycles, 7, 843–878,
https://doi.org/10.1029/93GB02263, 1993.

Takahashi, T., Sutherland, S. C., Sweeney, C., Poisson, A., Metzl, N., Tilbrook, B., Bates, N., Wanninkhof, R., Feely, R. A.,
Sabine, C., Olafsson, J., and Nojiri, Y.: Global sea-air CO2 flux based on climatological surface ocean pCO2, and seasonal
840 biological and temperature effects, Deep-Sea Research Part II: Topical Studies in Oceanography, 49, 1601–1622,
https://doi.org/10.1016/S0967-0645(02)00003-6, 2002.

Takahashi, T., Sutherland, S. C., Wanninkhof, R., Sweeney, C., Feely, R. A., Chipman, D. W., Hales, B., Friederich, G.,
Chavez, F., Sabine, C., Watson, A., Bakker, D. C. E., Schuster, U., Metzl, N., Yoshikawa-Inoue, H., Ishii, M., Midorikawa,
T., Nojiri, Y., Körtzinger, A., Steinhoff, T., Hoppema, M., Olafsson, J., Arnarson, T. S., Tilbrook, B., Johannessen, T., Olsen,
845 A., Bellerby, R., Wong, C. S., Delille, B., Bates, N. R., and de Baar, H. J. W.: Climatological mean and decadal change in

surface ocean pCO2, and net sea-air CO2 flux over the global oceans, Deep-Sea Research Part II: Topical Studies in Oceanography, 56, 554–577, https://doi.org/10.1016/j.dsr2.2008.12.009, 2009.

Takahashi, T., Sutherland, S. C., Chipman, D. W., Goddard, J. G., and Ho, C.: Climatological distributions of pH, pCO2, total CO2, alkalinity, and CaCO3 saturation in the global surface ocean, and temporal changes at selected locations, Marine
850 Chemistry, 164, 95–125, https://doi.org/10.1016/j.marchem.2014.06.004, 2014.

Telszewski, M., Chazottes, A., Schuster, U., Watson, A. J., Moulin, C., Bakker, D. C. E., González-Dávila, M., Johannessen, T., Körtzinger, A., Lüger, H., Olsen, A., Omar, A., Padin, X. A., Ríos, A. F., Steinhoff, T., Santana-Casiano, M., Wallace, D. W. R., and Wanninkhof, R.: Estimating the monthly pCO2 distribution in the north Atlantic using a self-organizing neural network, Biogeosciences, 6, 1405–1421, https://doi.org/10.5194/bg-6-1405-2009, 2009.

855 United Nations Environment Programme: Emissions Gap Report 2022: The Closing Window — Climate crisis calls for rapid transformation of societies, Nairobi, 1 pp., 2022.

Van Scoy, K. A., Olson, D. B., and Fine, R. A.: Ventilation of North Pacific intermediate waters: The role of the Alaskan Gyre, Journal of Geophysical Research: Oceans, 96, 16801–16810, https://doi.org/10.1029/91JC01783, 1991.

Wang, Y., Li, X., Song, J., Li, X., Zhong, G., and Zhang, B.: Carbon sinks and variations of pCO2 in the Southern Ocean from
860 1998 to 2018 based on a deep learning approach, IEEE Journal of Selected Topics in Applied Earth Observations and Remote Sensing, 14, 3495–3503, https://doi.org/10.1109/JSTARS.2021.3066552, 2021.

Wanninkhof, R.: Relationship between wind speed and gas exchange over the ocean revisited, Limnology and Oceanography: Methods, 12, 351–362, https://doi.org/10.4319/lom.2014.12.351, 2014.

Wanninkhof, R. and Triñanes, J.: The impact of changing wind speeds on gas transfer and its effect on global air-sea CO2
865 fluxes, Global Biogeochemical Cycles, 31, 961–974, https://doi.org/10.1002/2016GB005592, 2017.

Wanninkhof, R., Park, G.-H., Takahashi, T., Sweeney, C., Feely, R., Nojiri, Y., Gruber, N., Doney, S. C., McKinley, G. A., Lenton, A., Qu´er´e, C. L., Heinze, C., Schwinger, J., Graven, H., and Khatiwala, S.: Global ocean carbon uptake : magnitude , variability and trends, Biogeosciences, 10, 1983–2000, https://doi.org/10.5194/bg-10-1983-2013, 2013.

Weiss, R. F.: Carbon dioxide in water and seawater: the solubility of a non-ideal gas, Marine Chemistry, 2, 203–215,
870 https://doi.org/10.1016/0304-4203(74)90015-2, 1974.

Wong, C. S. and Chan, Y.-H.: Temporal variations in the partial pressure and flux of CO2 at ocean station P in the subarctic northeast Pacific Ocean, Tellus, 43B, 206–223, https://doi.org/10.1034/j.1600-0889.1991.00014.x, 1991.

Wong, C. S. and Johnson, W. K.: Subarctic Ecosystem Response to Iron Enrichment Study (SERIES): Eastern Subarctic Pacific, July 2002, Institute of Ocean Sciences, Sidney, B.C, 2002.

875 Wong, C. S., Christian, J. R., Emmy Wong, S. K., Page, J., Xie, L., and Johannessen, S.: Carbon dioxide in surface seawater of the eastern North Pacific Ocean (Line P), 1973-2005, Deep-Sea Research Part I: Oceanographic Research Papers, 57, 687–695, https://doi.org/10.1016/j.dsr.2010.02.003, 2010.

Xu, S., Park, K., Wang, Y., Chen, L., Qi, D., and Li, B.: Variations in the summer oceanic pCO 2 and carbon sink in Prydz Bay using the self-organizing map analysis approach, Biogeosciences, 16, 797–810, https://doi.org/10.5194/bg-16-797-2019,
880 2019.

Young, I. R. and Ribal, A.: Multiplatform evaluation of global trends in wind speed and wave height, Science, 364, 548–552, https://doi.org/10.1126/science.aav9527, 2019.

Yu, J., Wang, X., Fan, H., and Zhang, R. H.: Impacts of Physical and Biological Processes on Spatial and Temporal Variability of Particulate Organic Carbon in the North Pacific Ocean during 2003–2017, Scientific Reports, 9, 1–15, https://doi.org/10.1038/s41598-019-53025-4, 2019.

Zheng, C. W., Pan, J., and Li, C. Y.: Global oceanic wind speed trends, Ocean and Coastal Management, 129, 15–24, https://doi.org/10.1016/j.ocecoaman.2016.05.001, 2016.

Zhong, G., Li, X., Song, J., Qu, B., Wang, F., and Wang, Y.: Reconstruction of global surface ocean p CO 2 using region-specific predictors based on a stepwise FFNN regression algorithm, Biogeosciences, 19, 845–859, https://doi.org/10.5194/bg-19-845-2022, 2022.

885

890

Table 1 Northeast Pacific Open Ocean artificial neural network predictor variables, and their corresponding source, original temporal and spatial resoltuions, and processing steps used for this study.

Predictor variable	Source	Original resolution		Processing
		Temporal	**Spatial**	
Satellite-based product				
Sea surface temperature (SST)	SST_cci Level 4 Analysis Version 2.1	Daily	1/20°x1/20°	Averaged to monthly, aggregated to 1/12°x1/12°
Chlorophyll-*a* (Chl)	Ocean_Colour_cci Version 5.0	Daily	1/24°x1/24°	Averaged to monthly, aggregated to 1/12°x1/12°, log10-transformed
Satellite and in-situ observation data assimilated reanalysis product				
Sea surface salinity (SSS)	Copernicus Marine Service Global Reanalysis PHY_001_030	Monthly	1/12°x1/12°	None
Sea surface height (SSH)				None
Mixed layer depth (MLD)				log10-transformed
Atmospheric-measurement-based interpolation product				
Atmospheric $p$$xCO_2$	Landschützer et al. (2020) - NCEI Accession 0160558	Monthly	1°x1°	Interpolated to 1/12°x1/12°
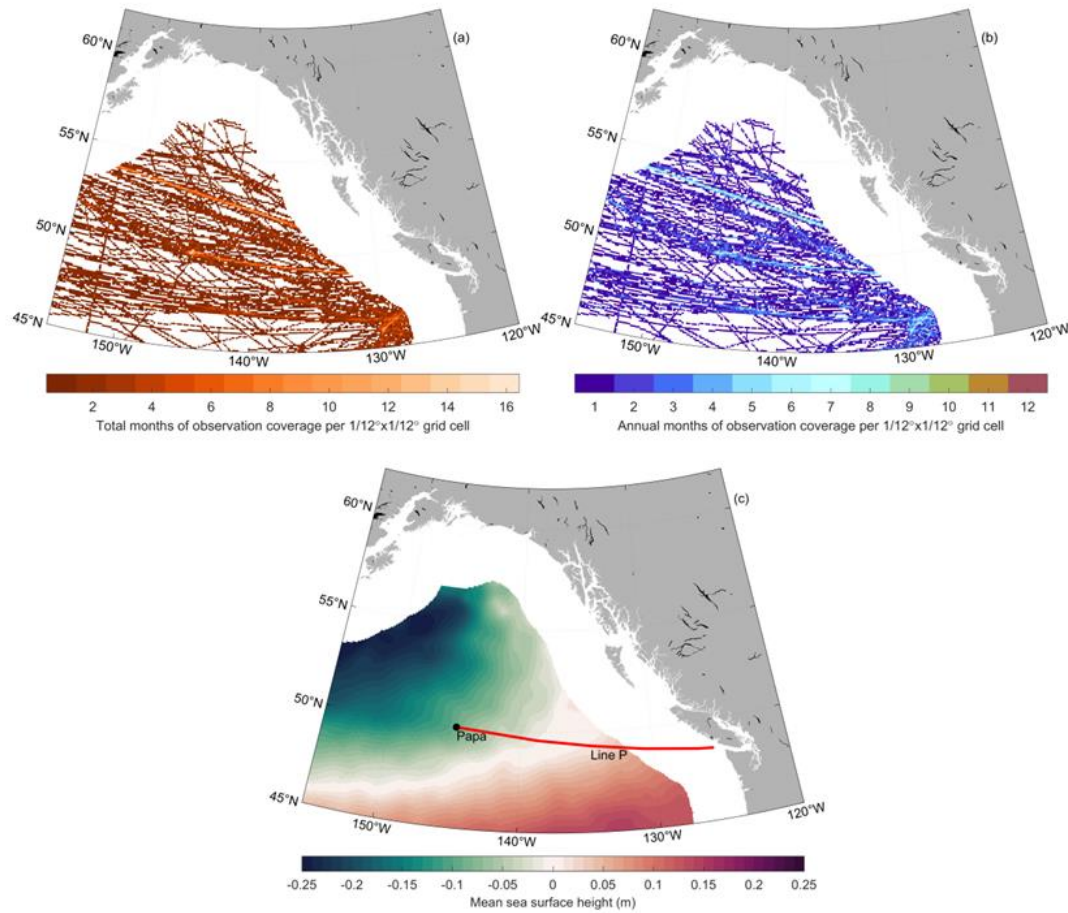
Figure 1 (a) Total number of months of observational coverage from Surface Ocean CO₂ Atlas (SOCAT) v2021 (Bakker et al., 2016) and additional data from Fisheries and Oceans Canada February 2019 Line P cruise (https://www.waterproperties.ca/linep/) per 1/12°x1/12° grid cell. (b) Number of unique annual months of observational coverage per 1/12°x1/12° grid cell. (c) Mean sea surface height (SSH; Table 1) shows relative location of the subpolar Alaskan Gyre (negative SSH values), and the North Pacific Current (SSH approximately equal to zero). Ocean Station Papa is labeled and marked with a black circle while Line P is labelled and marked with a red line.

900
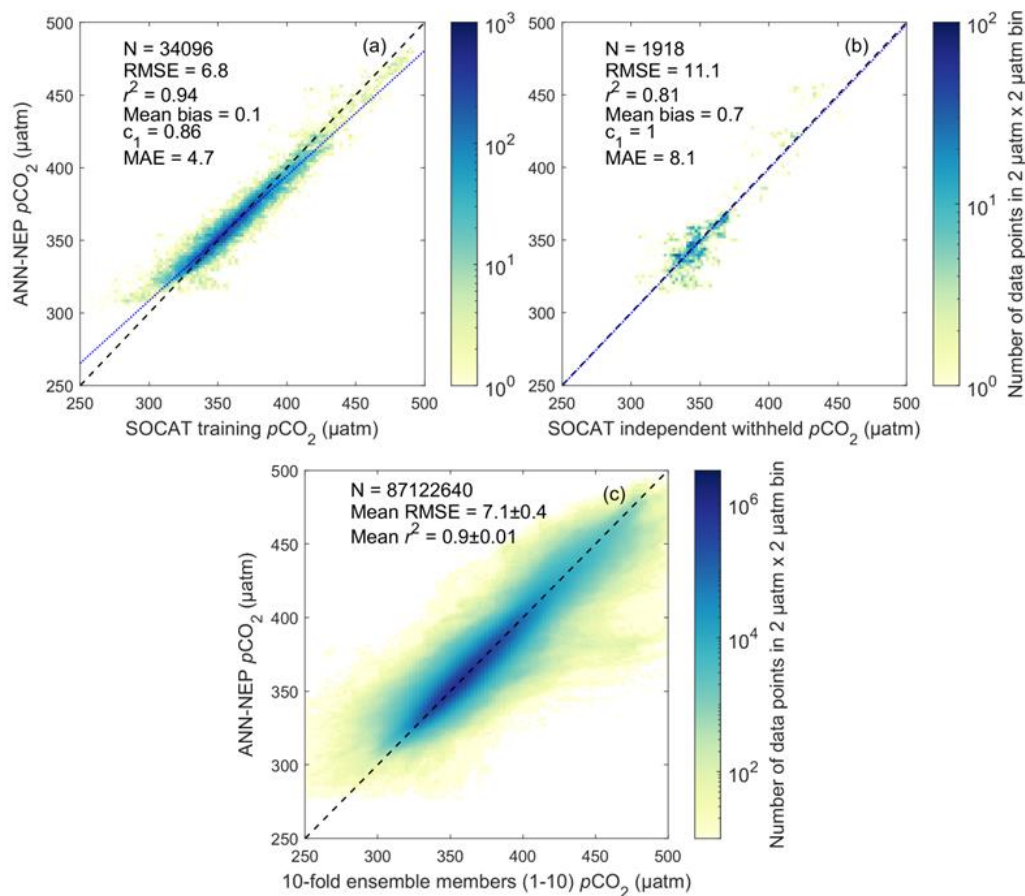
Figure 2 Regional high-resolution artificial neural network Northeast Pacific (ANN-NEP) ensemble mean pCO_2 against (a) training pCO_2 observation data, and (b) independent withheld pCO_2 observation data. Number of observations (N), root mean squared error (RMSE), coefficient of determination (r^2), mean absolute error (MAE), mean bias (calculated as the mean residual), and the slope of the linear regression (c_1). The observed linear relationship is represented by the dotted blue line. (c) ANN-NEP pCO_2 (ensemble mean) against individual ensemble member estimates. Total number of observations (N) across all 10-fold ensemble members (see Section 2.5). Across all panels data are binned into 2 µatm by 2 µatm bins. The dashed black line represents a perfect fit of slope (c_1) = 1 and intercept = 0. Colorbar shows data density on a log scale. Note the order of magnitude difference in the colorbar scale between panels.
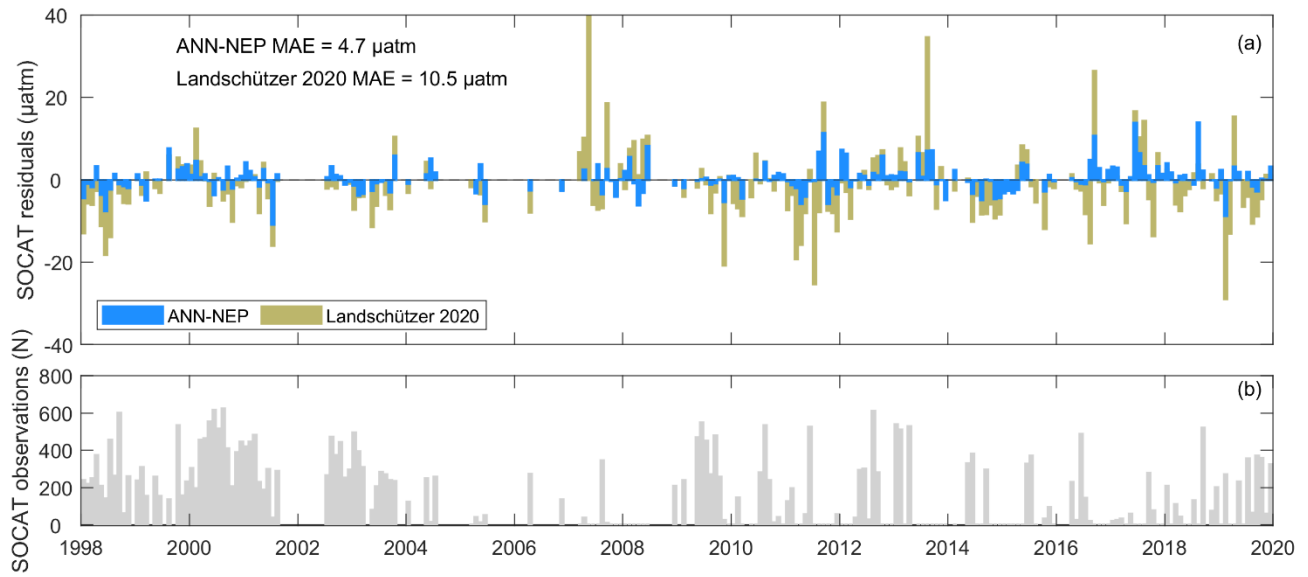
Figure 3 (a) Mean residuals over the full study area at each timestep of the ANN-NEP *p*CO₂ estimate in this study, the Landschützer et al. (2020b) product interpolated to the 1/12°x1/12° grid of this study, compared to the gridded SOCAT data displaying the mean absolute error (MAE). (b) total number of gridded SOCAT observations across the study area at each timestep.

915
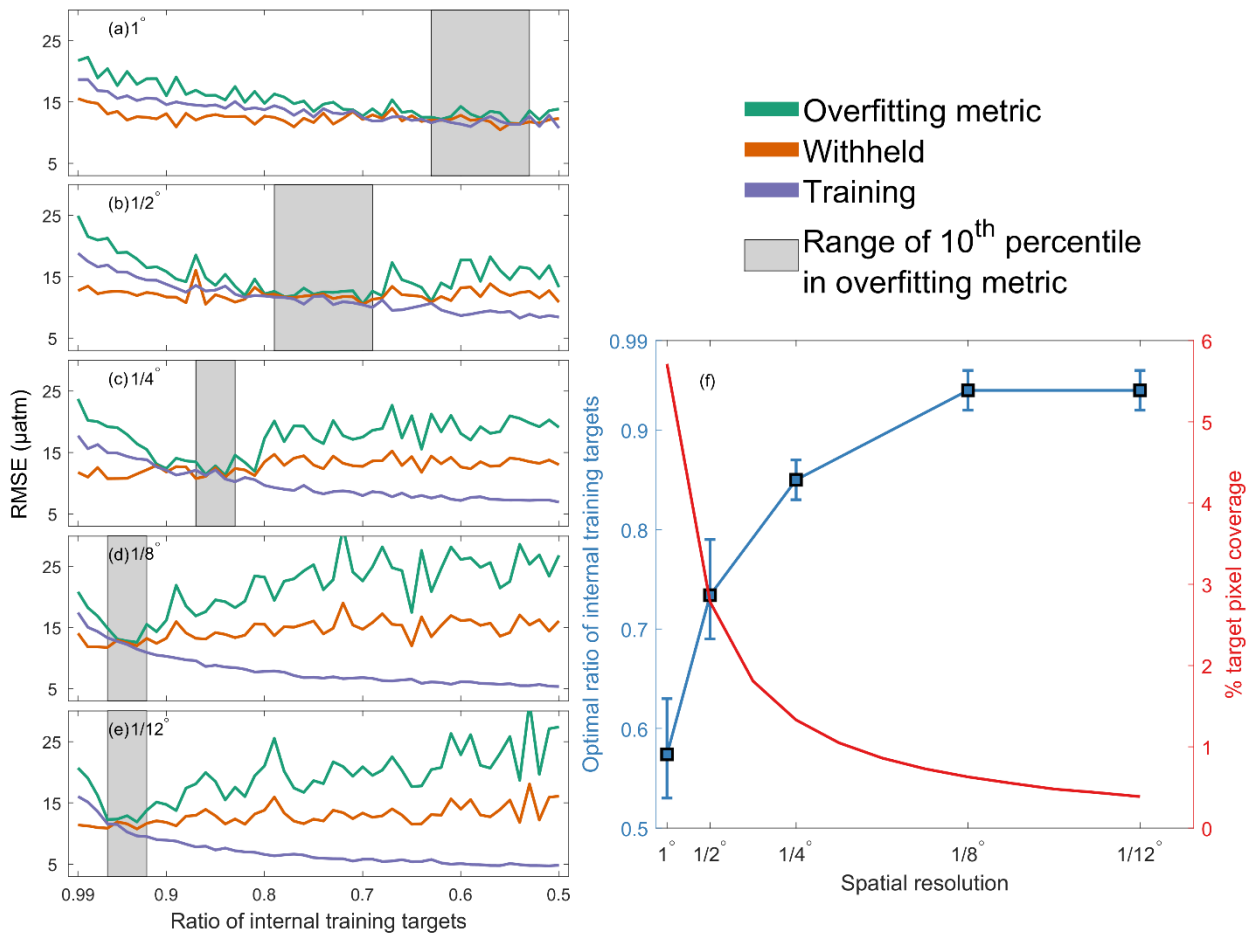
Figure 4 Varying spatial resolution: (a) 1°, (b) 1/2°, (c) 1/4°, (d) 1/8°, and (e) 1/12° ANN pCO₂ product performance evaluated by the mean RMSE (Section 2.3) of training data (blue line), independently withheld data (orange line), and an overfitting metric (green line; Section 3.4) against internal data division ratios between the pCO₂ training data used by the ANN to train and internally evaluate. The ratios in grey show the range of the lower 10th percentile (5 of 50 runs) of overfitting metric values for each resolution. (f) At each spatial resolution, the lefthand y-axis shows the optimal internal data division ratio with error bars representing the lower 10th percentile of overfitting metric values (same as grey ranges in (a) to (e) with all resolutions converging around RMSE = 12.8±0.4 µatm). The righthand y-axis shows the percent of gridded pCO₂ observations (targets) compared to the total number of grid cells.
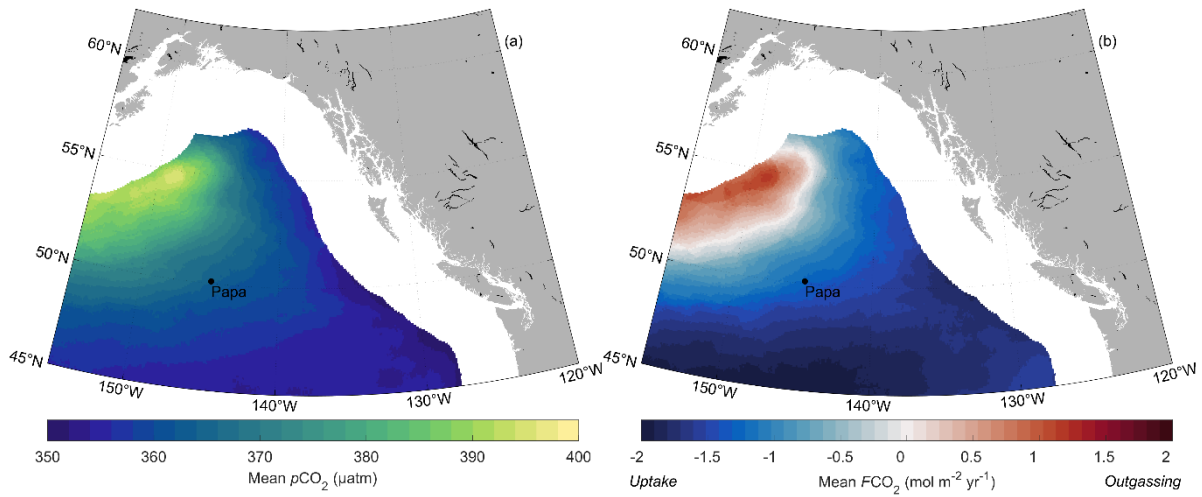
Figure 5 (a) Long-term (1998-2019) mean ANN-NEP pCO_2 and **(b)** CO_2 flux density in mol m^{-2} yr^{-1} for the open ocean Northeast Pacific. Negative (positive) flux values indicate CO_2 uptake (outgassing) by the ocean. Ocean Station Papa is shown for reference.
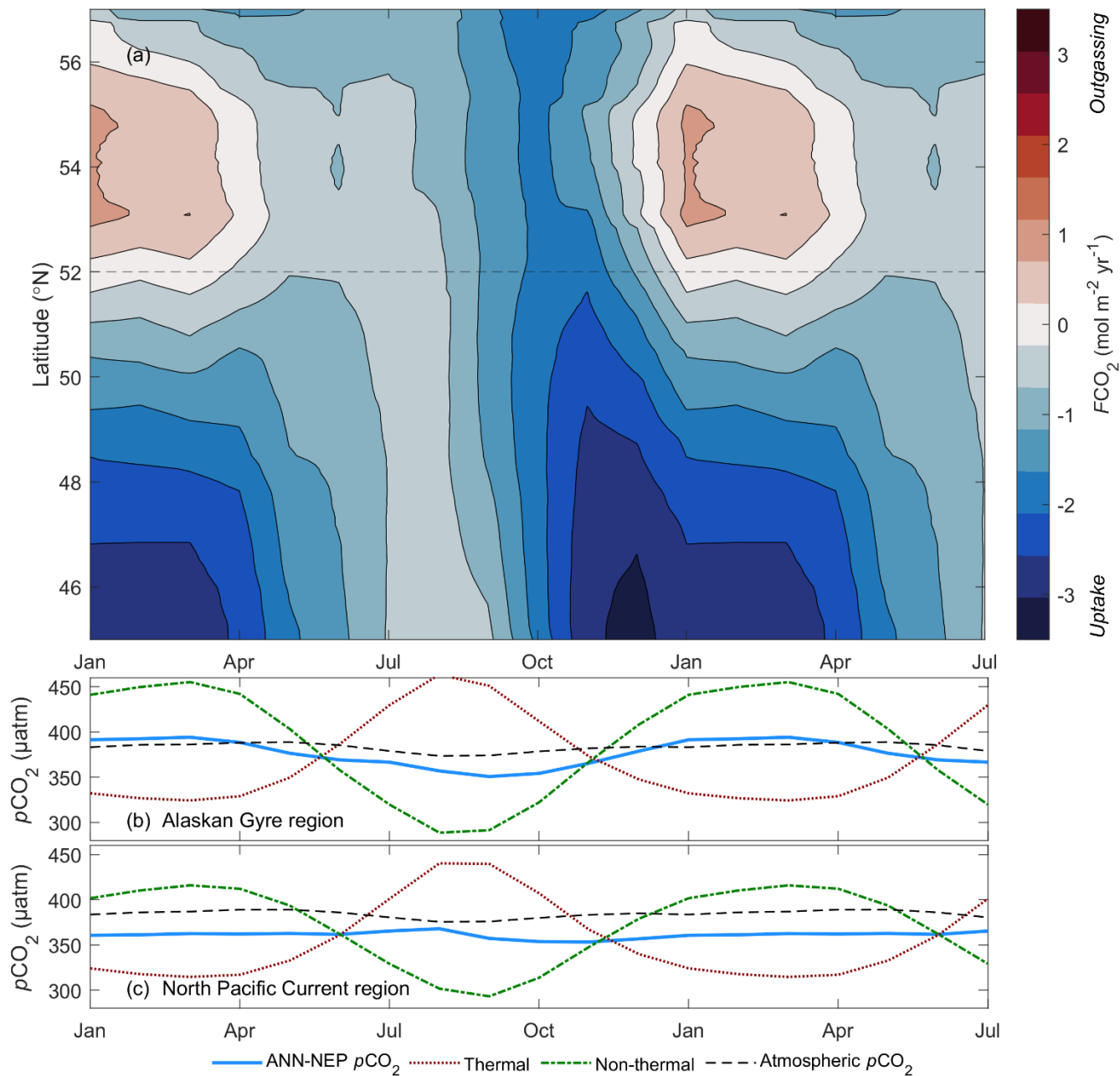
Figure 6 (a) Zonally averaged air-sea CO₂ flux from the ANN estimated *p*CO₂ product climatology along each 1/12° latitude band in the study area plotted against the climatological month along the x-axis (Hovmöller diagram). Negative (positive) flux values indicate CO₂ uptake (outgassing) by the ocean. The dashed grey line subdivides the Alaskan Gyre and North Pacific Current regions in the North/South with different seasonal drivers summarized in panels below. (b) Alaskan Gyre region (latitudes north of 52°N) & (c) North Pacific Current region (latitudes south of 52°N) area averaged monthly climatological *p*CO₂ (solid blue line), thermal component (i.e., changes due to temperature; Eq. 4; dotted red line), non-thermal component (i.e., changes due to circulation, mixing, gas exchange, and biology; Eq. 5; dot-dash green line), and atmospheric *p*CO₂ (dashed black line). The climatology is plotted over 19 months to emphasize the seasonal cycle.
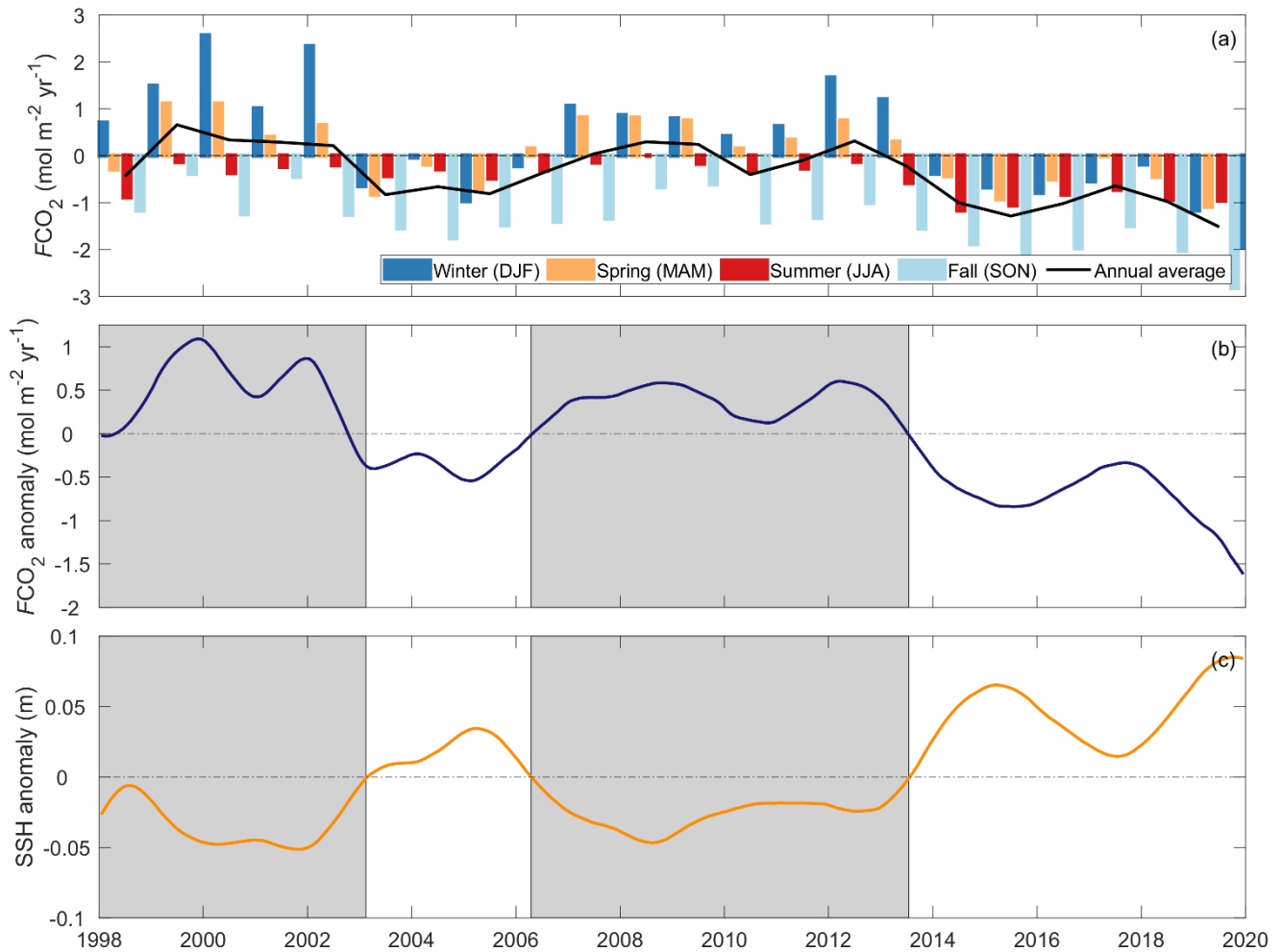
Figure 7 Alaskan Gyre region of our study area (latitudes north of 52° N). (a) Air-sea CO₂ fluxes grouped by seasonal three-month bins along with the annual average (black line). (b) Air-sea CO₂ flux anomalies removing the seasonal cycle (Section 2.4) and applying a 12-month running mean. (c) Sea surface height (SSH) anomalies in the same region removing the seasonal cycle and applying a 12-month running mean. Grey boxes highlight periods of anomalously high Alaskan Gyre upwelling strength corresponding to negative SSH anomalies. Horizontal dashed lines mark zero in each panel. Seasonal groupings in (a) are winter (December, January, February), spring (March, April, May), summer (June, July, August), fall (September, October, November).
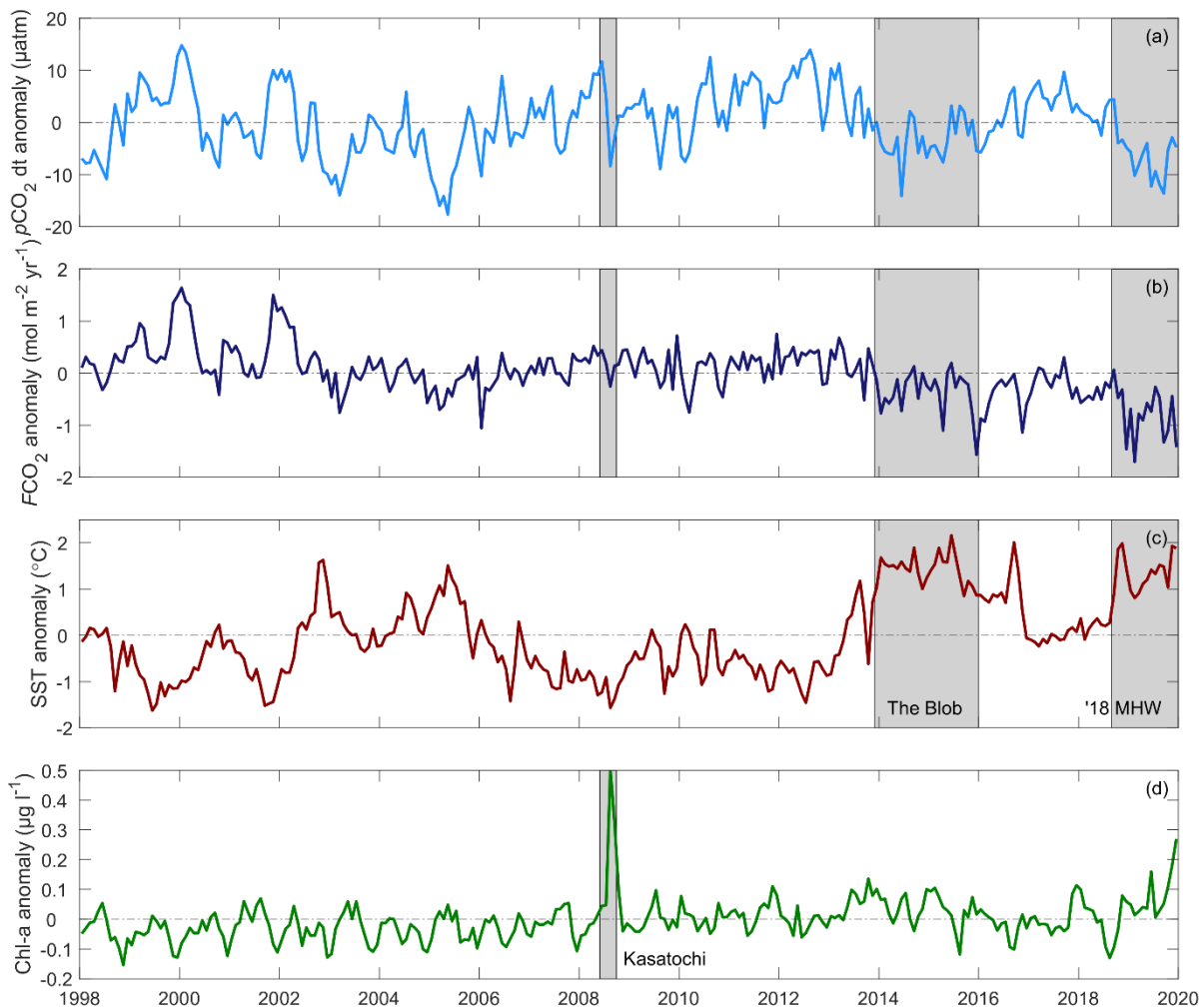
945

Figure 8 Full study area-averaged interannual variability in (a) $p\text{CO}_2$ anomaly removing the seasonal cycle (Section 2.4) and long-term trend (Section 4.4), (b) air-sea CO_2 flux anomaly, (c) sea surface temperature anomaly, and (d) chlorophyll-a anomaly all removing the seasonal cycle. Grey boxes highlight large interannual events including "The Blob" marine heatwave 2014-2016, a second marine heatwave 2018-2020 ('18 MHW), and a 2008 ocean iron fertilization event following the Kasatochi volcanic eruption
950 (Kasatochi). Horizontal dashed lines mark zero in each panel.
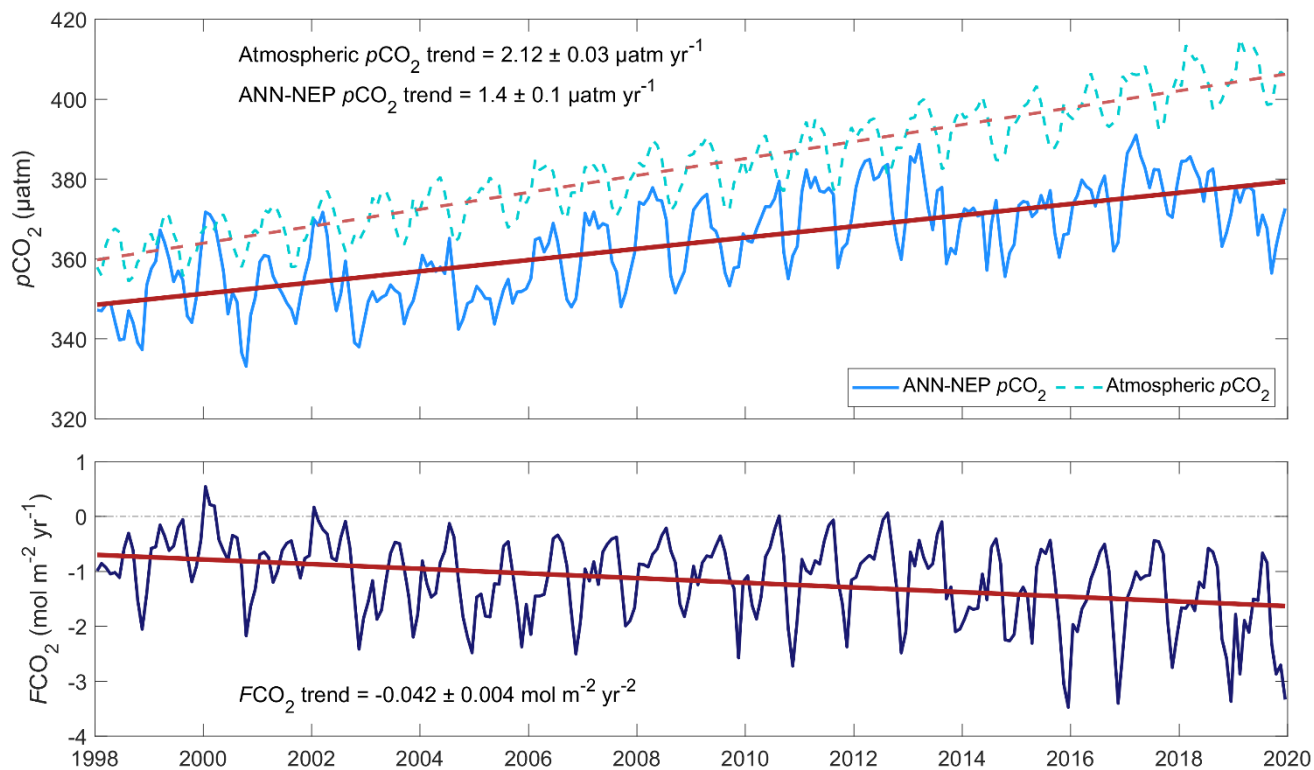
Figure 9 Full study area-averaged long-term trends in (a) ANN-NEP surface ocean *p*CO₂ (solid line) and atmospheric *p*CO₂ (dashed line), and (b) air-sea CO₂ flux.
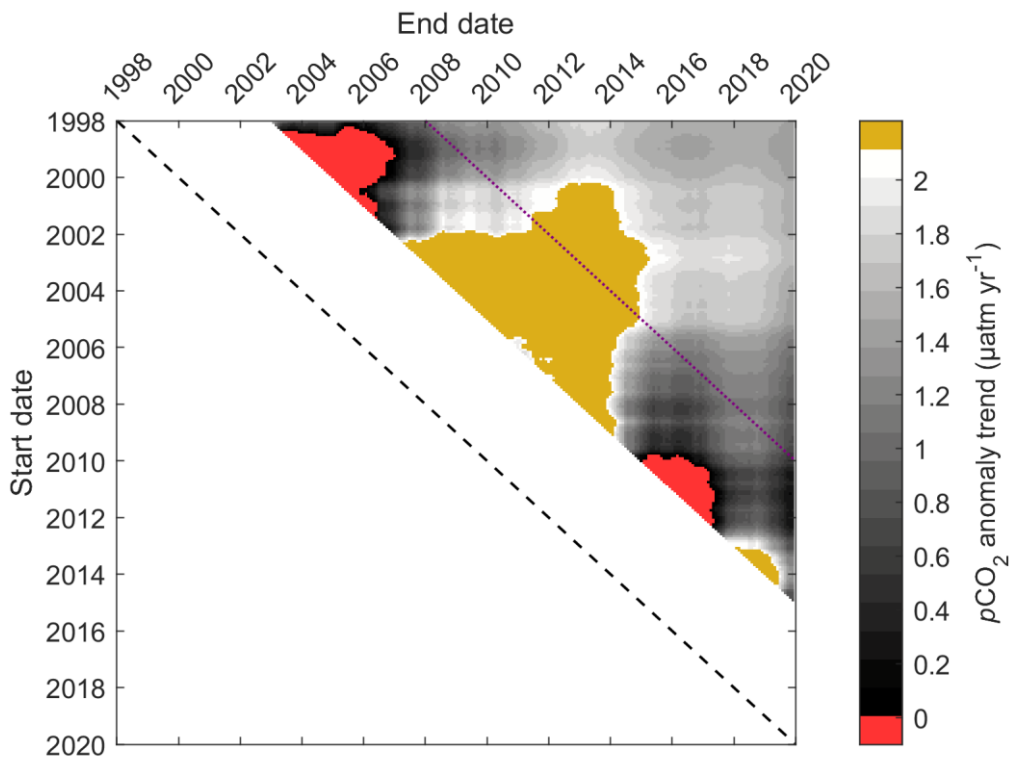
955 **Figure 10 Full study area-averaged pCO$_2$ anomaly (removing the seasonal cycle; Section 2.4) linear trend calculated using different monthly timeseries endpoints. Timeseries start from dates on the left and end on a date along the top. The dashed black line indicates equal start and end dates. Trend values are only shown for timeseries of at least a 5-year duration. Red values represent negative pCO$_2$ trends, gold values represent trends greater than the atmospheric rate of increase (2.12±0.01 μatm yr^{-1}). The purple dotted line indicates a 10-year timeseries duration.**

960
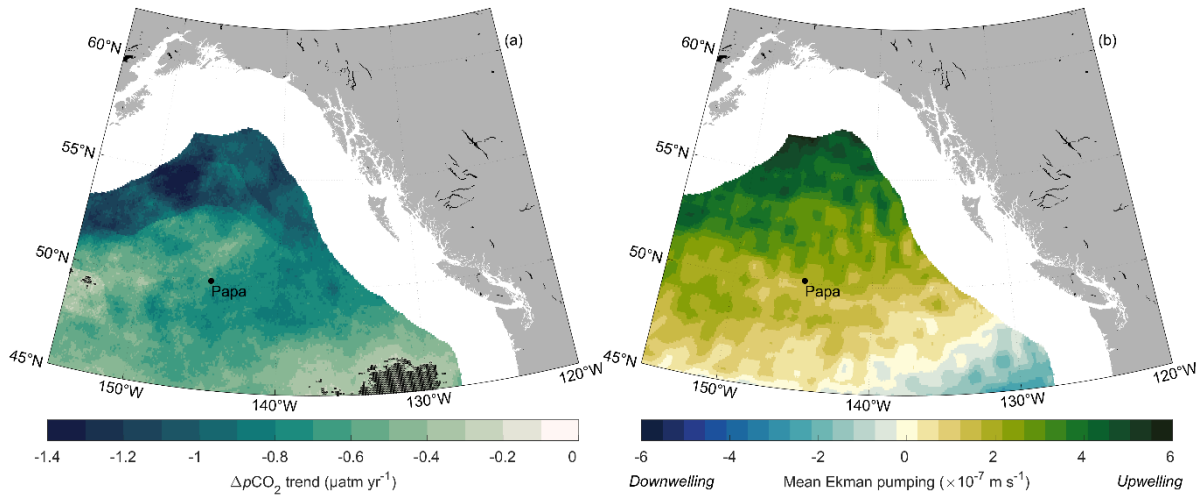
Figure 11 (a) Trend in Δ*p*CO₂ where more negative (darker) values indicate an increasing gradient with the atmosphere and a lag in the *p*CO₂ increase in the surface ocean. Black crosshatches show grid cells with an insignificant calculated trend (outside the 95% confidence level; p ≥0.05). (b) Calculated average vertical velocity associated with Ekman pumping (calculated from zonal and meridional wind speed) where negative (blue) values indicate downwelling and positive (green) values indicate upwelling. Ocean Station Papa is shown for reference.